Diffuse flow hydrothermal manganese mineralization along the active Mariana and southern Izu-Bonin arc system, western Pacific

James R. Hein,[1] Marjorie S. Schulz,[1] Rachel E. Dunham,[1] Robert J. Stern,[2] and Sherman H. Bloomer[3]

Received 10 October 2007; revised 25 February 2008; accepted 10 March 2008; published 25 June 2008.

[1] Abundant ferromanganese oxides were collected along 1200 km of the active Izu-Bonin-Mariana arc system. Chemical compositions and mineralogy show that samples were collected from two deposit types: Fe-Mn crusts of mixed hydrogenetic/hydrothermal origin and hydrothermal Mn oxide deposits; this paper addresses only the second type. Mn oxides cement volcaniclastic and biogenic sandstone and breccia layers (Mn sandstone) and form discrete dense stratabound layers along bedding planes and within beds (stratabound Mn). The Mn oxide was deposited within coarse-grained sediments from diffuse flow systems where precipitation occurred below the seafloor. Deposits were exposed at the seabed by faulting, mass wasting, and erosion. Scanning electron microscopy and microprobe analyses indicate the presence of both amorphous and crystalline 10 Å and 7 Å manganate minerals, the fundamental chemical difference being high water contents in the amorphous Mn oxides. Alternation of amorphous and crystalline laminae occurs in many samples, which likely resulted from initial rapid precipitation of amorphous Mn oxides from waxing pulses of hydrothermal fluids followed by precipitation of slow forming crystallites during waning stages. The chemical composition is characteristic of a hydrothermal origin including strong fractionation between Fe (mean 0.9 wt %) and Mn (mean 48 wt %) for the stratabound Mn, generally low trace metal contents, and very low rare earth element and platinum group element contents. However, Mo, Cd, Zn, Cu, Ni, and Co occur in high concentrations in some samples and may be good indicator elements for proximity to the heat source or to massive sulfide deposits. For the Mn sandstones, Fe (mean 8.4%) and Mn (12.4%) are not significantly fractionated because of high Fe contents in the volcaniclastic material. However, the proportion of hydrothermal Fe (nondetrital Fe) to total Fe is remarkably constant (49–58%) for all the sample groups, regardless of the degree of Mn mineralization. Factor analyses indicate various mixtures of two dominant components: hydrothermal Mn oxide for the stratabound Mn and detrital aluminosilicate for the Mn-cemented sandstone; and two minor components, hydrothermal Fe oxyhydroxide and biocarbonate/biosilica. Our conceptual model shows that Mn mineralization was produced by hydrothermal convection cells within arc volcanoes and sedimentary prisms that occur along the flanks and within calderas. The main source of hydrothermal fluid was seawater that penetrated through fractures, faults, and permeable volcanic edifices. The fluids were heated by magma, enriched in metals by leaching of basement rocks and sediments, and mixed with magmatic fluids and gases. Dikes and sills may have been another source of heat that drove small-scale circulation within sedimentary prisms.

Citation: Hein, J. R., M. S. Schulz, R. E. Dunham, R. J. Stern, and S. H. Bloomer (2008), Diffuse flow hydrothermal manganese mineralization along the active Mariana and southern Izu-Bonin arc system, western Pacific, *J. Geophys. Res.*, *113*, B08S14, doi:10.1029/2007JB005432.

1. Introduction

[2] Iron oxyhydroxides and manganese oxides are ubiquitous in the deep ocean and form generally by three processes [*Hein*, 2004]: (1) Accretion of Fe-Mn colloids from ambient bottom seawater onto hard rock substrates produces hydrogenetic deposits, (2) precipitation from sediment pore fluids

[1] U.S. Geological Survey, Menlo Park, California, USA.
[2] Geosciences Department, University of Texas at Dallas, Richardson, Texas, USA.
[3] College of Science, Oregon State University, Corvallis, Oregon, USA.

0148-0227/08/2007JB005432$09.00

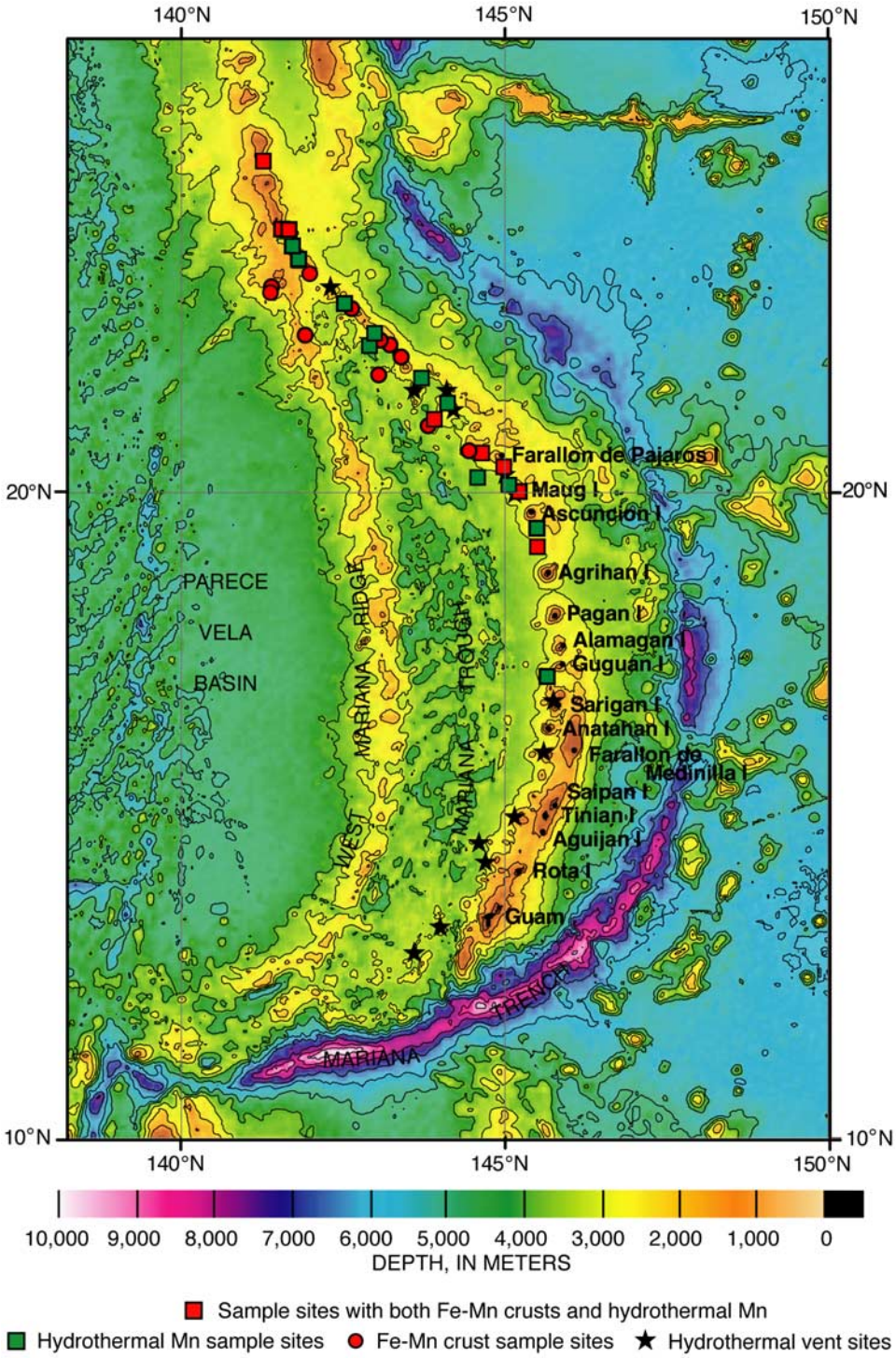

Figure 1. Shaded bathymetric map of the Mariana Island arc system and sample locations for cruise TT192 (filled squares and circles) and hydrothermal vent sites (stars) taken from NOAA cruises in 2003 and 2004 (http://oceanexplorer.noaa.gov/explorations/04fire; and other papers in this special section). Contour interval is 1000 m.

below and from seawater above produces mixed diagenetic/hydrogenetic deposits, and (3) precipitation of either relatively pure Mn oxides or Fe oxyhydroxides from ascending hydrothermal fluids produces stratabound hydrothermal deposits.

[3] Hydrothermal Mn oxides from the active Mariana volcanic arc are the focus of this paper (Figure 1 and Table 1). These diffuse flow hydrothermal precipitates are the distal products of the hydrothermal systems that produce proximal polymetallic massive sulfides and sulfates.

Table 1. Dredge Locations and Depths for Samples in Table 2, Cruise TT192

	Location	Latitude (N)	Longitude (E)	Depth (m)
D3	SW Guguan Ridge	17° 09.65′	145° 39.25′	2975-2860
D8	Poyo seamount	19° 09.74′	145° 30.20′	2880-2200
D11	Cheref seamount	19° 27.52′	145° 29.86′	1380-894
D12	Maug caldera	20° 01.36′	145° 13.12′	172-55
D13	Supply Reef	20° 07.03′	145° 03.57′	1650-1060
D15	Ahyi seamount	20° 23.91′	144° 58.85′	1930-1120
D20	NW Uracas Seamount	20° 36.84′	144° 38.82′	1640-1510
D28	Cross Chain Seamount	21° 07.96′	143° 54.79′	1715-1350
D31	Eifuku seamount	21° 23.44′	144° 06.85′	1715-1500
D33	Kasuga seamount	21° 46.22′	143° 42.83′	1170-600
D40	Syoyo seamount	22° 16.45′	142° 54.67′	1635-1390
D41	Syoyo Ridge	22° 28.09′	142° 59.39′	1230-600
D44	Ichiyo seamount	22° 55.94′	142° 31.54′	2000-1760
D47	N. Hiyoshi seamount	23° 23.35′	141° 59.42′	2030-1600
D51	Central Hiyoshi Knoll	23° 35.00′	141° 49.20′	1400-1060
D52	Central Hiyoshi Knoll	23° 37.08′	141° 48.81′	1105-647
D54	N. Hiyoshi seamount	23° 49.25′	141° 43.25′	1640-1250
D55	SW Fukutoku seamount	24° 02.50′	141° 35.60′	1780-1070
D56	NW Fukutoku seamount	24° 04.80′	141° 33.45′	1500-1250
D57	SE Fukutoku seamount	24° 04.25′	141° 39.85′	1730-930
D73	Kita Io-Jima	25° 07.70′	141° 16.10′	1620-1240

The hydrothermal Mn oxides precipitated below the seafloor as stratabound oxide layers and as cement for volcaniclastic and biogenic sediments. On discharge of the hydrothermal fluids from the seafloor, Fe-Mn crusts of mixed hydrothermal/hydrogenetic origin were precipitated. These Fe-Mn crusts of mixed origin were also recovered from the Mariana arc and are used here for comparative purposes.

2. Geographic and Geologic Settings

[4] The Mariana volcanic arc forms the southern third of the Izu-Bonin-Mariana (IBM) arc system, a 2600-km-long arc-trench system in which the Pacific plate plunges beneath the Philippine Sea plate and into the Earth's mantle along the IBM trench. The chain of volcanic seamounts and islands is located about 200 km west of the trench axis. The IBM started to develop about 54 Ma, and volcanic activity has occurred at various places along the arc since that time. West of the IBM volcanic arc is the mostly sediment-covered floor of the eastern Philippine Sea, with numerous seamounts, ridges, and basins with ages mainly less than 42 Ma. The basins and ridges consist of (1) the Mariana Trough, an active back-arc spreading center located immediately west of the Mariana arc, (2) the West Mariana Ridge, a remnant (extinct) volcanic arc, and (3) the Parece Vela Basin abyssal plain (Figure 1).

[5] The geologically continuous IBM volcanic arc is divided politically into three parts, The U.S. Territory of Guam in the southernmost Marianas, the U.S. Commonwealth of the Northern Mariana Islands (CNMI) in the central and northern Marianas, and the Japanese Izu-Bonin islands in the north. The volcanic front in the Japan sector is delineated by the Izu Islands to the north, Nishinoshima Island in the central region, and the Volcano Islands (the most notable being Iwo Jima) to the south, near the junction with the Mariana Islands. A group of older islands that occur in the fore-arc region of the Japanese sector are referred to both as the Bonin and Ogasawara islands; these islands are similar to the tectonically uplifted islands in the southern Mariana arc (Saipan to Guam).

[6] The CNMI consists of 14 islands (477 km^2 total area) that delineate a 483-km-long archipelago (Figure 1). This archipelago sits atop the Mariana ridge, which extends about 1200 km within the Exclusive Economic Zone (EEZ) of CNMI and 167 km within the Guam EEZ. South of Guam, the Mariana ridge breaks up into a series of seamounts and basins until it joins the Yap arc at nearly a 90° angle. Many seamounts occur on the Mariana ridge between the islands. Six islands have been volcanically active during historic times: Pagan, Agrihan, Asuncion, Farallon de Pajaros, Guguan, and Anatahan. In addition, at least 20 volcanic centers along the chain are volcanically or hydrothermally active [*Baker et al.*, 2008].

3. Samples and Methods

[7] Samples were collected during cruise TT192 aboard the R/V *T. Thompson* in 1985 (Figure 1 and Table 1), a cruise dedicated primarily to the study of the petrologic and geochemical evolution of the Mariana volcanic arc [*Bloomer et al.*, 1989a, 1989b; *Lin et al.*, 1989]. This study is therefore based on random sampling of volcanoes distributed along about 1200 km of the active arc. Hydrogenetic, hydrothermal, and mixed hydrogenetic/hydrothermal Fe/Mn oxide samples were collected [*Hein et al.*, 1987; *Schulz and Hein*, 1991]. The composition, textures, and mechanisms of formation of the hydrothermal samples are presented here. Individual samples are labeled using the dredge number (e.g., D1) and a rock designation number (e.g., D1-1, D1-2, etc.).

[8] Chemical analyses were completed on 61 samples of Mn-cemented sandstone and stratabound Mn, and two samples of a magnetite-goethite-siderite rock (Table 2) from 21 dredge hauls. Major oxides were determined by X-ray fluorescence (XRF) spectrometry on samples D47-2A through D47-2D and D54-4; for all other samples most major and minor elements were determined by inductively coupled plasma–atomic emission spectrometry (ICP-AES), except for K, Zn, and Pb which were determined by flame atomic–absorption spectroscopy, and As, Cr, and Cd by graphite-furnace atomic absorption spectroscopy on air-dried samples [*Aruscavage et al.*, 1989]. Concentrations of rare earth elements (REEs) were determined by ion exchange chemical separation and ICP-AES, and platinum-group elements by fire assay and ICP–mass spectrometry [*Lichte et al.*, 1987a, 1987b]. Fe(II) was determined for selected samples using modulated potential pulse coulometry and Hg by cold vapor spectrometry. Abundances of CO_2 were determined by coulometric titration [*Engleman et al.*, 1985], H_2O^+ by water evolved at 950°C as determined coulometrically by Karl-Fischer titration [*Jackson et al.*, 1987], and H_2O^- by sample weight difference on heating to 110°C for more than 1 h [*Shapiro*, 1975].

[9] Major elements were also determined by microprobe on doubly polished thin sections using an ARL-SEMQ nine-spectrometer electron microprobe [*Schulz and Hein*, 1991]. Volcanic glass and manganese oxides were analyzed using a defocused beam (~50 μm) with an accelerating voltage of 15 kV and sample current of 10 nA. Counting

Table 2. Chemical Composition of Bulk Hydrothermal Mn and Fe Samples From IBM Cruise TT192[a]

	Group 1																	
	D8-1	D8-5A	D8-12A	D8-12B	D8-12C	D8-20	D13-1A	D15-1A	D28-3A	D28-4A	D28-6A	D31-1	D33-2-1	D33-2-2	D33-2-3A	D40-3A	D40-3B	D40-3C
Fe	8.22	17.6	12.6	5.83	15.4	4.76	4.76	16.5	6.70	4.93	5.71	4.90	13.2	26.5	9.03	4.00	4.65	5.50
Mn	9.95	12.9	14.0	4.50	7.40	12.0	12.3	9.44	5.69	16.3	15.9	7.86	20.4	18.2	14.9	9.53	15.2	16.1
Fe/Mn	0.827	1.37	0.904	1.30	2.08	0.395	0.385	1.75	1.18	0.302	0.359	0.623	0.649	1.46	0.607	0.419	0.306	0.342
Si	17.8	10.9	14.4	20.0	15.8	17.9	18.6	15.9	21.1	16.1	15.7	21.1	10.8	6.71	–	24.8	19.2	16.5
Na	1.30	1.74	1.66	2.16	1.70	2.19	2.48	1.52	2.03	2.18	2.16	2.35	1.84	1.06	–	2.74	2.51	2.18
Al	0.406	3.78	4.21	8.09	5.52	6.58	6.98	5.08	7.72	5.95	5.82	7.45	3.63	1.18	3.18	6.05	6.34	6.24
Mg	6.70	1.69	2.05	1.84	1.54	2.71	0.364	0.965	0.487	0.585	0.735	2.63	1.64	1.24	1.32	1.44	2.39	2.76
Ca	6.29	3.46	2.77	8.70	3.54	6.68	6.38	3.32	6.29	5.13	5.31	5.92	2.81	0.988	2.05	3.38	3.70	4.12
K	0.416	0.661	1.17	0.573	1.05	0.860	0.364	0.965	0.487	0.585	0.735	1.15	1.02	0.871	0.86	0.676	0.866	0.835
Ti	0.416	0.850	0.298	0.450	0.917	0.324	0.354	0.280	0.386	0.349	0.418	0.378	0.209	0.061	0.144	0.369	0.338	0.349
P	0.044	0.315	0.144	0.066	0.281	0.075	0.029	0.166	0.057	0.040	0.055	0.112	0.165	0.308	<0.025	0.041	0.039	0.050
LOI	–	–	–	–	–	–	–	–	–	–	–	6.40	19.2	18.1	–	8.00	11.6	12.8
H_2O^-	1.50	4.70	2.60	2.30	4.00	1.20	1.20	3.60	1.50	2.60	2.00	2.00	9.20	5.90	2.60	2.40	5.30	5.40
H_2O^+	1.83	6.61	5.54	1.94	6.35	2.23	2.43	5.50	1.62	3.80	3.88	4.39	7.60	10.1	–	3.59	3.27	4.44
CO_2	0.010	0.189	0.051	3.21	0.198	0.840	0.435	0.083	0.020	0.770	0.949	0.367	0.165	0.085	–	0.256	0.063	0.053
As	10.2	189	92.4	13.3	125	12.1	<2	187	12.2	14.4	19.4	3.06	132	850	–	9.22	16.9	23.3
Ba	254	1154	2875	266	917	294	233	882	315	637	908	622	826	2338	524	686	1584	2960
Cd	8.53	6.09	6.37	1.74	1.98	0.658	0.354	1.92	0.457	7.60	16.3	<0.1	1.16	1.38	0.31	4.51	8.76	9.73
Ce	9.14	325	54.4	<10	219	223	<10	17.6	<10	52.4	<10	71.4	<60	<60	<10	22.5	22.2	10.6
Co	50.8	976	760	18.4	552	142	27.3	187	42.6	33.9	52.0	19.4	617	1169	<5	33.8	56.0	76.1
Cr	142	21.0	35.9	21.5	25.0	71.9	39.5	27.0	86.3	8.21	8.67	85.7	29.7	10.4	6.67	14.3	22.2	29.6
Cu	213	609	4107	123	417	911	223	135	142	98.6	194	71.4	176	372	46	174	370	550
Li	–	–	–	–	–	–	–	–	–	–	–	–	–	–	–	–	–	–
Mo	74.1	147	236	<5	19.8	56.7	38.5	197	<5	68.8	71.4	<5	804	404	226	154	158	180
Ni	325	1259	1437	133	760	121	38.5	270	54.8	58.5	306	21.4	330	138	71	225	475	518
Pb	<50	682	308	<50	344	<50	<50	<50	<50	<50	<50	<50	<50	<50	<50	<50	54.9	60.3
Sr	213	1049	554	420	833	405	304	373	294	370	429	724	452	499	421	256	327	412
V	467	609	318	266	354	223	253	239	264	329	469	204	72.7	149	329	143	180	233
Y	17.3	136	40.0	38.9	115	97.2	17.2	20.7	17.3	46.2	34.7	15.3	18.7	22.3	35.9	26.6	34.8	40.2
Zn	315	588	493	143	385	84.0	86.0	228	112	113	398	163	297	223	329	266	454	560
Hg	<20	–	<20	<20	–	20	–	–	20	–	–	–	–	–	<20	–	–	–
Pd	2.0	2.3	2.5	2.7	2.3	4.0	5.7	2.7	4.7	2.5	4.7	–	–	–	–	–	–	–
Pt	5.1	88	27	7.2	41	6.1	<5	18	7.1	11	8.2	–	–	–	–	–	–	–
Rh	<1	<1	<1	<1	<1	<1	<1	<1	<1	<1	<1	–	–	–	–	–	–	–
Thickness (mm)	40	60	10	12	8	15	5	8	–	70	20	5	8	–	20	30	15	17
Type	Mn-SS	Mn-SS	Mn-SS	Mn-SS	Mn-SS	Mn-SS	Mn-SS	Mn-SS	Mn-SS	Mn-SS	Mn-SS	Mn-SS	Mn-SS	Mn-breccia	Mn-breccia	Mn-breccia	Mn-breccia	Mn-SS

Table 2. (continued)

	Group 1											Subgroup 2A										
	D47-2A	D47-2B	D47-2C	D47-2D	D54-2	D55-3	D56-1B	D57-2	D57-4	D73-1A	D12-2	D44-1	D44-1A	D44-3	D51-1	D52-4A	D52-4C	D52-5	D52-9A	D52-11	D54-4	D56-2
Fe	6.30	6.54	6.35	6.33	6.69	4.53	5.45	9.56	5.70	6.57	2.84	5.76	5.96	2.41	2.00	6.80	3.49	6.74	3.78	4.02	5.27	1.67
Mn	8.33	7.19	8.92	7.94	14.9	15.9	16.1	20.9	10.7	13.0	29.8	37.0	35.8	38.8	35.2	31.0	27.9	37.4	35.4	41.0	26.9	28.4
Fe/Mn	0.757	0.910	0.711	0.797	0.448	0.284	0.338	0.457	0.533	0.504	0.095	0.156	0.167	0.062	0.057	0.220	0.125	0.180	0.107	0.098	0.196	0.059
Si	19.7	20.4	19.6	20.0	15.3	16.9	15.1	12.6	17.7	17.3	10.5	7.53	8.05	6.48	6.26	8.41	10.2	5.65	6.67	5.23	10.6	7.11
Na	2.32	2.36	2.41	2.44	2.02	2.52	2.26	2.04	1.71	2.51	2.28	3.32	3.93	3.35	2.81	1.86	2.36	2.15	1.99	3.06	1.82	2.53
Al	8.54	8.78	8.36	8.68	6.28	6.07	6.27	3.57	7.43	5.85	4.12	0.874	1.31	1.85	2.85	2.66	4.32	0.107	2.39	1.35	4.82	2.74
Mg	2.53	2.51	2.43	2.37	3.30	2.05	2.50	2.22	3.56	2.31	2.32	1.22	1.18	1.81	2.44	2.11	2.39	1.54	2.31	1.36	3.64	1.96
Ca	6.83	6.83	6.57	6.75	5.25	3.81	4.73	2.49	6.71	4.11	3.71	1.34	1.71	1.68	2.91	2.07	3.19	1.65	2.06	2.21	3.84	7.97
K	0.639	0.659	0.720	0.715	1.53	2.09	1.70	1.68	1.04	0.975	0.804	0.970	0.762	1.08	1.37	1.68	1.94	1.50	1.71	0.913	0.834	1.13
Ti	0.417	0.427	0.422	0.430	0.443	0.309	0.360	0.168	0.305	0.431	0.196	0.047	0.071	0.106	0.148	0.146	0.236	0.077	0.136	0.109	0.346	0.135
P	0.143	0.093	0.098	0.098	0.103	0.092	0.123	0.137	0.072	0.081	0.040	<0.025	<0.025	<0.025	0.062	0.115	0.092	0.171	0.080	0.076	0.089	0.050
LOI	8.44	4.66	5.36	5.74	–	–	–	–	–	–	–	–	20.3	20.2	–	–	–	–	–	19.9	–	–
H_2O^-	5.15	1.80	1.94	2.43	2.90	2.80	2.70	4.80	1.70	2.60	3.00	6.20	9.40	7.00	5.10	4.40	2.70	6.50	4.70	8.00	6.48	3.40
H_2O^+	0.980	1.78	2.26	2.01	4.02	3.60	6.17	5.78	2.85	3.59	5.46	6.08	6.73	8.28	5.80	6.80	6.06	6.95	7.24	7.72	5.76	5.59
CO_2	0.063	0.051	0.051	0.072	0.031	0.021	0.606	0.021	0.010	0.144	0.062	0.011	0.066	0.043	1.58	0.042	0.031	0.032	0.021	0.011	0.160	6.11
As	–	–	–	–	14.4	18.5	24.7	65.1	22.4	20.5	38.1	53.3	48.6	25.8	35.8	59.6	21.6	105	52.5	69.6	–	20.7
Ba	–	–	–	–	1030	1132	678	1050	804	472	1546	1812	1071	785	917	2301	596	1390	1364	870	–	942
Cd	–	–	–	–	9.89	22.6	14.4	12.6	2.14	8.21	18.6	<0.2	<0.1	5.05	10.5	10.3	6.06	<0.2	7.24	8.15	–	4.35
Ce	–	–	–	–	40.2	64.8	75.0	32.6	15.3	<10	<10	14.9	<10	19.4	9.48	18.8	18.5	22.5	28.3	44.6	–	14.5
Co	–	–	–	–	34.0	20.6	62.7	231	224	31.8	12.4	181	82.8	215	46.4	91.0	36.0	246	105	293	–	41.4
Cr	–	–	–	–	14.4	17.5	11.3	17.9	78.3	5.95	15.5	1.60	2.21	2.15	2.11	2.62	12.3	7.49	4.72	4.35	–	4.14
Cu	–	–	–	–	206	134	216	80.9	315	164	134	320	210	441	63.2	70.1	103	66.3	65.1	66.3	–	45.5
Li	–	–	–	–	–	–	–	–	–	–	–	–	–	–	–	–	–	–	–	–	–	–
Mo	–	–	–	–	85.5	56.6	65.8	252	142	87.3	247	714	673	763	263	241	504	567	441	717	–	104
Ni	–	–	–	–	175	247	349	315	112	175	155	139	105	183	158	220	195	299	283	228	–	75.6
Pb	–	–	–	–	23.7	28.8	56.5	21.0	<10	20.5	<50	16.0	<50	<50	19.0	29.3	44.2	40.6	45.1	65.2	–	20.7
Sr	–	–	–	–	824	648	699	504	631	441	546	299	287	355	611	732	514	556	577	467	–	642
V	–	–	–	–	319	195	247	179	214	318	639	<5	<5	25.8	169	136	59.6	<5	61.9	<5	–	83.9
Y	–	–	–	–	19.6	22.6	25.7	14.7	13.2	25.7	12.4	8.53	7.73	10.5	9.48	13.6	16.4	10.7	12.6	9.13	–	13.5
Zn	–	–	–	–	227	360	411	221	112	298	165	37.3	<50	108	200	188	216	150	210	120	–	88.0
Hg	–	–	–	–	–	–	–	–	–	–	–	–	–	–	–	–	–	–	–	–	–	–
Pd	–	–	–	–	–	2.3	–	–	–	–	2.1	3.0	–	–	1.3	–	–	1.3	–	–	–	–
Pt	–	–	–	–	–	5.1	–	–	–	–	10	14	–	–	<5	–	–	<5	–	–	–	–
Rh	–	–	–	–	–	<1	–	–	–	–	<1	<1	–	–	<1	–	–	<1	–	–	–	–
Thickness (mm)	20	34	32	48	15	30	30	15	25	90	~1	20	10	34	42	20	20	60	40	10	40	40
Type	Mn-SS	Mn-breccia	Mn-SS	Mn-breccia	Mn-SS	Mn-SS	Mn-SS	Mn-SS	Mn-SS	Mn-SS	Mn-SS	SB-Mn w/rx	SB-Mn inclw/rx	SB-Mn inclw/rx	Mn-SS inclw/SB-Mn	Mn-SS w/SB-Mn	Mn-SS w/SB-Mn	Mn-SS w/SB-Mn	Mn-SS w/SB-Mn	SB-Mn w/sed incl	Mn-breccia	Mn-SS w/SB-Mn

Table 2. (continued)

	Subgroup 2B																						
	D3-1	D3-3	D3-5	D8-8	D11-1A	D20-1A	D28-1B	D28-1-CI	D28-1-CII	D28-1D	D28-1E	D28-1F	D28-1G	D33-2-3	D41-2B	D52-4B	D52-9B	D52-10	D55-4	D56-4	D73-1F	D12-1	D12-1A
Fe	0.401	0.241	0.741	0.643	1.62	0.526	1.05	0.719	0.368	0.118	0.104	0.109	1.30	4.69	1.16	0.177	2.76	1.38	0.117	0.081	0.362	28.6	37.1
Mn	49.3	50.3	46.5	42.9	46.1	47.7	47.5	49.8	48.0	49.6	50.8	49.5	44.2	43.7	47.2	49.3	41.9	48.4	47.0	50.7	48.1	0.877	0.566
Fe/Mn	0.008	0.005	0.016	0.015	0.035	0.011	0.022	0.014	0.008	0.002	0.002	0.002	0.029	0.107	0.025	0.004	0.066	0.028	0.002	0.002	0.008	32.6	65.4
Si	1.26	0.598	2.17	1.53	2.04	1.69	1.30	0.606	0.491	0.111	0.182	0.244	2.91	1.54	1.12	0.190	4.15	1.71	0.199	0.051	0.433	4.93	3.42
Na	3.81	3.66	3.69	2.37	1.60	3.37	2.33	2.83	2.97	2.37	2.56	2.83	1.90	1.46	1.80	2.48	2.69	2.63	2.20	2.20	2.18	0.651	0.645
Al	0.438	0.304	0.940	1.11	0.864	0.588	0.529	0.327	0.325	0.129	0.119	0.240	1.49	0.543	0.608	0.115	1.36	0.495	0.149	0.329	0.543	1.61	1.23
Mg	0.976	0.713	1.01	2.95	1.83	0.526	2.56	2.15	2.03	2.65	2.21	1.83	2.22	1.87	2.30	2.07	1.81	1.55	2.56	2.46	2.18	2.43	1.39
Ca	2.22	2.23	2.38	1.75	1.11	2.43	1.62	1.59	1.65	1.49	1.53	1.73	1.78	1.03	1.47	1.54	1.91	1.74	1.80	1.77	1.71	9.81	5.02
K	0.325	0.419	0.465	1.05	1.61	0.526	1.21	0.980	0.791	1.25	1.02	0.795	1.05	1.50	1.65	1.09	1.08	0.914	1.75	0.988	1.12	<0.12	0.026
Ti	0.025	0.019	0.048	0.051	0.101	0.037	0.077	0.038	0.028	<0.01	0.030	<0.01	0.095	0.030	0.037	0.009	0.097	0.038	0.011	<0.01	0.026	0.090	0.095
P	<0.025	<0.025	0.45	<0.025	0.059	<0.025	0.106	0.142	0.206	0.118	0.089	0.185	0.070	0.080	0.033	<0.025	0.094	0.043	0.028	<0.025	<0.025	0.051	0.028
LOI	–	–	34.0	25.7	–	–	23.9	25.0	25.8	24.6	24.3	24.8	21.7	23.2	–	–	20.3	21.3	–	24.1	–	22.0	–
H_2O^-	20.1	4.60	9.60	8.20	3.90	3.00	7.40	8.20	7.70	7.00	7.40	8.20	6.80	6.10	6.20	4.20	6.40	7.00	5.90	8.90	6.00	4.20	5.66
H_2O^+	9.26	7.23	11.2	11.2	7.70	7.84	7.78	9.26	8.88	8.39	9.18	10.1	8.80	9.90	7.78	8.98	9.19	9.03	7.12	9.99	8.19	6.68	5.99
CO_2	0.075	0.042	0.044	0.065	0.062	0.041	0.043	0.065	0.054	0.054	0.086	0.120	0.129	0.724	0.032	0.021	0.085	0.065	0.043	0.110	0.319	16.08	10.8
As	109	147	122	44.7	114	113	41.0	52.3	45.5	34.4	41.0	69.7	53.6	75.6	83.2	29.2	49.1	51.6	51.0	46.1	55.3	50.1	74.2
Ba	864	524	774	1307	5203	464	713	708	488	645	972	1307	2468	2236	2239	553	983	1075	956	1866	5319	32.4	27.6
Cd	2.38	1.47	0.774	34.9	16.6	2.84	34.6	39.2	36.8	39.8	75.6	86.1	53.6	4.58	24.5	0.522	6.41	2.69	13.8	14.3	3.03	1.46	3.18
Ce	<60	2.10	<60	<60	22.9	<10	33.5	18.5	<10	<10	<10	12	<10	<60	19.2	<10	15.0	<10	<10	<10	4.26	<60	<4
Co	36.3	26.2	36.5	33.8	88.4	9.28	140	69.7	15.2	<5	3.37	<5	105	501	33.0	198	92.9	77.4	42.5	<5	6.81	15.7	36.0
Cr	<1	3.67	5.31	2.51	6.04	<2	1.62	1.09	2.49	<1	<1	<1	2.47	7.24	2.67	<1	2.67	4.30	<1	1.65	2.66	9.19	105
Cu	16.3	29.4	22.1	272	416	40.2	983	730	888	376	248	436	815	138	128	18.8	55.6	31.2	128	59.3	45.7	115	132
Li	–	–	227	616	–	148	–	–	–	–	1054	–	–	–	–	–	–	–	–	–	528		
Mo	801	1363	1007	359	874	1010	421	501	477	505	454	534	569	905	1279	637	321	548	553	252	309	<5	30.7
Ni	58.8	86.0	67.5	534	874	124	1026	534	693	215	162	251	891	554	384	31.3	182	105	361	132	57.4	710	142
Pb	<50	10.5	<50	<50	104	72.2	151	142	119	161	162	120	62.2	<50	32.0	<10	72.6	<50	10.6	<50	<10	<50	6.36
Sr	476	419	420	545	1145	371	486	468	412	484	508	556	547	703	725	470	545	581	627	746	606	1357	662
V	<5	<5	42.6	545	427	30.9	292	349	260	312	356	392	290	75.6	139	<5	105	<5	159	307	819	81.4	68.9
Y	<5	3.14	<5	27.2	39.5	<5	21.6	22.9	21.7	17.2	18.4	29.4	25.8	18.1	64.0	<5	10.7	<5	7.33	<5	23.4	5.22	<5
Zn	138	115	122	458	874	742	6263	8388	13109	7419	5616	12092	7296	426	469	18.8	182	69.9	276	98.8	53.2	99.2	17.0
Hg	–	17	–	–	–	<20	–	–	–	–	–	29	–	–	<20	<20	–	–	21	–	<20	–	21
Pd	–	<10	–	–	16	1.0	–	–	–	–	–	–	–	–	1.1	–	–	–	–	–	7	–	–
Pt	–	<5	–	–	56	<5	–	–	–	–	–	–	–	–	8.5	–	–	–	–	–	16	–	–
Rh	41	<1	27	–	<1	<1	–	–	–	–	–	–	–	–	<1	–	–	–	–	–	<1	–	–
Thickness (mm)	~9.5	~29	~27.5	4	15	15	5	7	3	5	6	12	40	~2	40	15	4	10	30	25	30	60 × 50 × 45	45 × 25 × 20
Type	SB-Mn	SB-Mn	SB-Mn	SB-Mn in Mn-SS	SB-Mn in repl-SS	SB-Mn	SB-Mn	SB-Mn	SB-Mn	SB-Mn	SB-Mn	SB-Mn	SB-Mn	SB-Mn in breccia	SB-Mn	SB-Mn	SB-Mn from 9A	SB-Mn	SB-Mn	SB-Mn	SB-Mn	magnetite-siderite-goethite nodule	magnetite-siderite-goethite nodule

[a]Loss on ignition (LOI) and H_2O^- as reported, all other values normalized to 0% hygroscopic water. Sulfur is reported at 4% for sample D11-1A. Li data from *Chan and Hein* [2007]. Mn-SS, Mn-cemented sandstone; SB-Mn, stratabound Mn; rx incl, host rock inclusions; sed include, sediment inclusions; repl-SS, completely replaced rock. Major elements are in percent (or weight percent), minor elements are in ppm, and Hg and platinum group elements are in ppb.

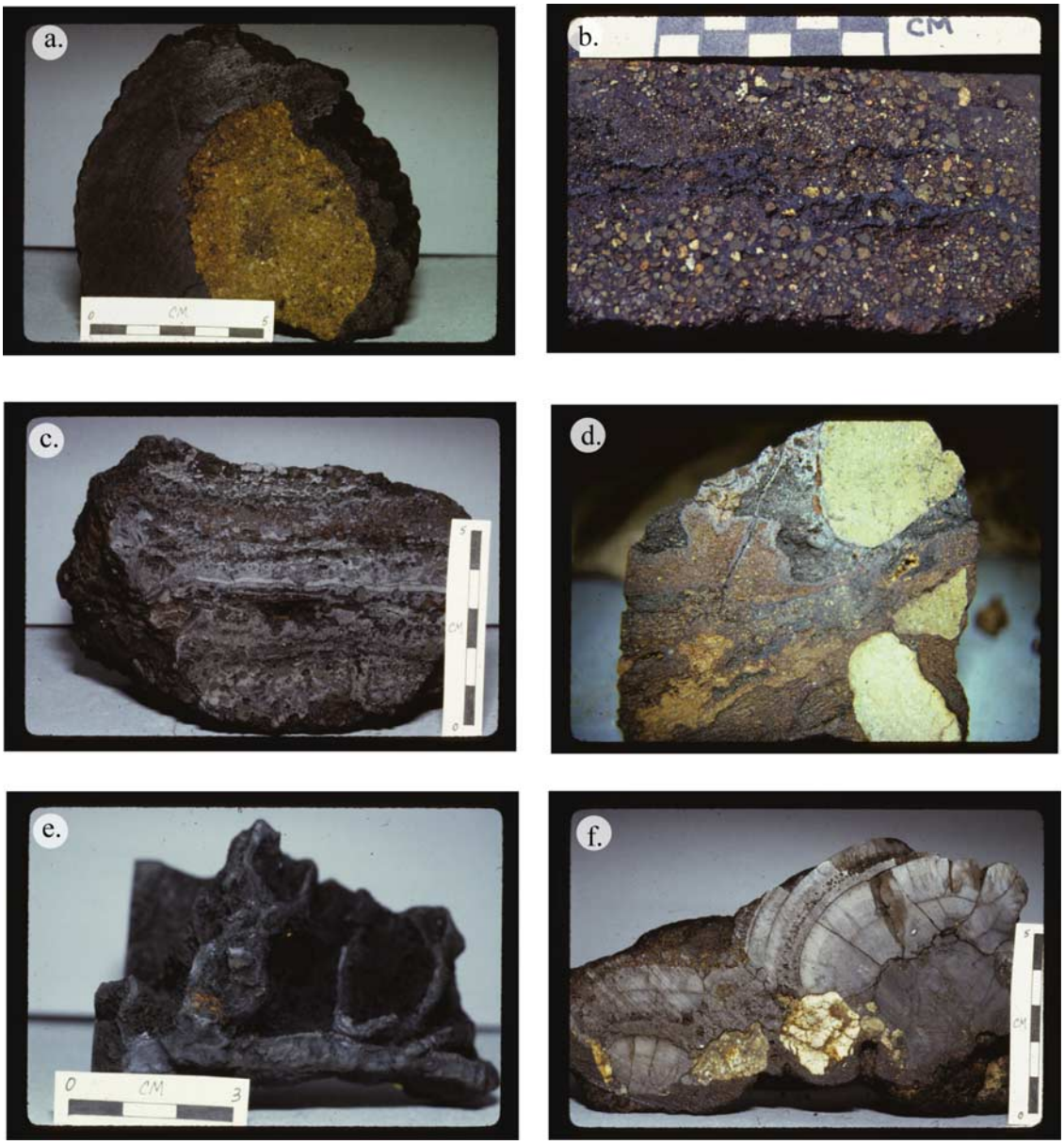

Figure 2. (a) Mixed hydrogenetic/hydrothermal Fe-Mn crust, D59-4; (b) coarse-grained Mn oxide cemented sandstone with submetallic gray stratabound Mn oxide stringers, D41-1; (c) metallic gray stratabound Mn oxide bed with multiple layers, D52-5; (d) breccia with gray Mn oxide veins, vug fill, and cement, D33-2-3. (e) metallic gray hydrothermal Mn oxide cobble that was coated with red mud when collected, D3-1; (f) layers of metallic gray, dense, hydrothermal Mn oxide; the seven layers analyzed are strongly enriched in Zn, from 0.6 to 1.3 wt %, D28-1. Note centimeter scales.

times were 10 s. All raw microprobe data were reduced on line with a modified version of the Bence-Albee method [*Albee and Ray*, 1970].

[10] X-ray diffraction (XRD) analyses were performed on all Fe/Mn samples analyzed for chemical composition as well as the host rocks [*Hein et al.*, 1987] using a Norelco generator with Cu Kα radiation at 40 kV and 20 mA, with a curved crystal graphite monochromator. Petrography was performed on doubly polished thin sections using transmitted and reflected light. Scanning electron microscopy (SEM) investigations were performed on polished thin sections and fracture surfaces of selected samples. Samples were carbon coated and imaged using backscatter and secondary electrons. Semiquantitative chemical analyses were undertaken using an energy dispersion X-ray analyzer (EDX).

[11] The Pearson product moment correlation coefficient was used to calculate correlation coefficient matrices. For Q-mode factor analysis, each variable percentage was scaled to the percent of the maximum value before the values were normalized by row and the cosine theta coefficients calculated. The factors were derived from orthogonal rotations of the principal component eigenvectors using the Varimax method [*Klovan and Imbrie*, 1971].

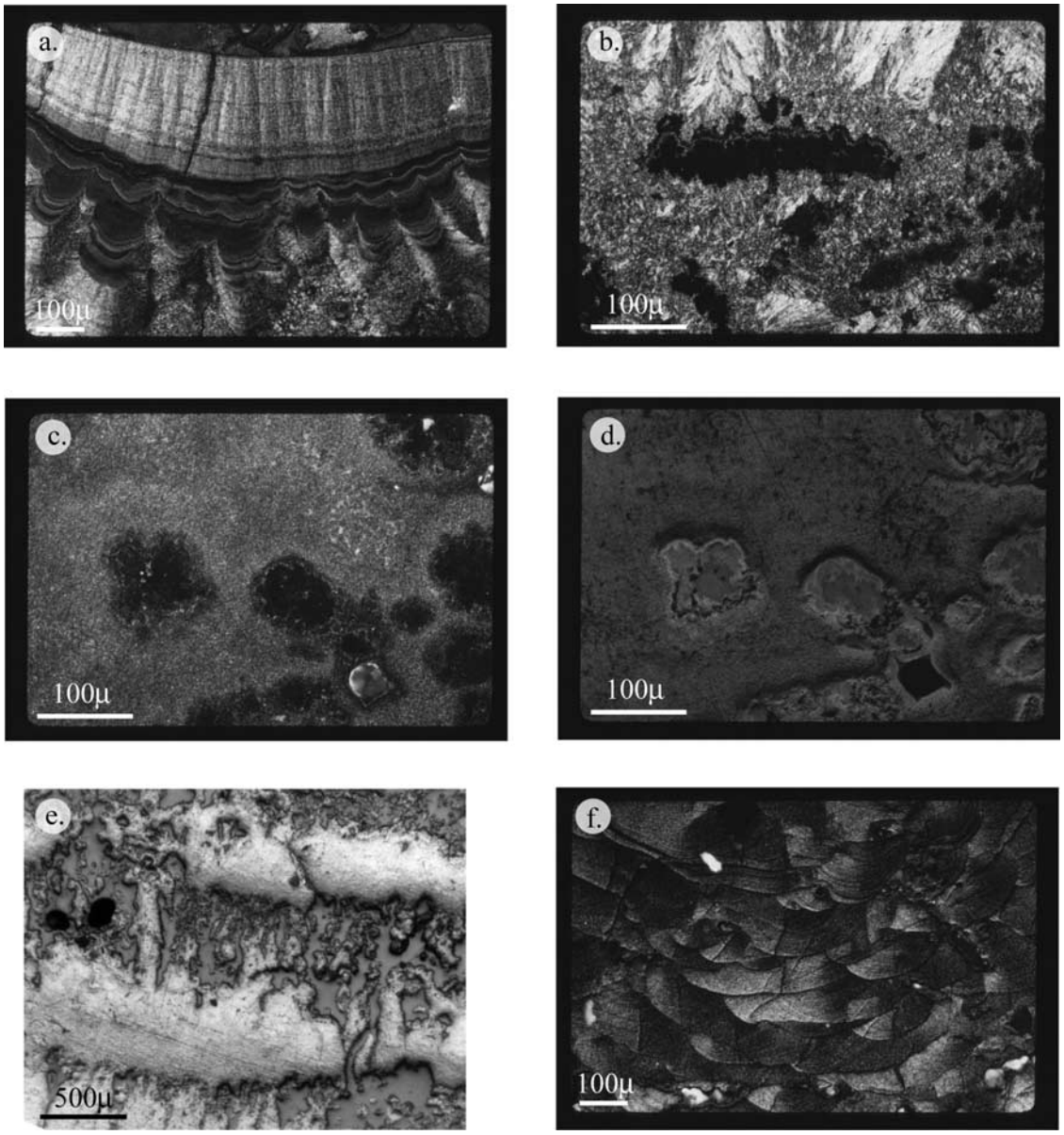

Figure 3. Thin section photomicrographs: (a) aligned crystallites within botryoidal and underlying colloform amorphous cryptocrystalline oxides; as mineralization continued, botryoids were overgrown by radially aligned crystallites extending downward into the sediment, D28-2; (b) mosaic crystallites nucleating on amorphous cryptocrystalline (AC) cores; at top of photo are larger plumose crystallites, D3-3; (c, d) microcrystalline Mn oxides precipitated around AC Mn oxides (dark areas), in polarized reflected light (Figure 3c) and plane-reflected light (Figure 3d) showing apparent relief that AC oxides display, D28-4; (e) alternating fibrous porous and dense laminae; reflected and transmitted light, D3-3; (f) scalloped texture, D28-2.

All communalities are $\geq$0.9. Low factor scores ($\leq|0.15|$) were discarded because they are not statistically significant.

4. Results

[12] Eighty-four dredge attempts resulted in 66 that recovered rock samples. Of those 66 dredge hauls, 18 (27%) contained significant amounts of Fe/Mn deposits and 22 (33%) contained some Fe/Mn oxides. Host rocks for the hydrothermal Mn oxides include volcaniclastic rocks, breccia, mixed volcaniclastic/foraminiferal sandstone, and minor foraminiferal limestone. The volcaniclastic rocks are mostly sandstone but range from mudstone to conglomerate.

[13] Five varieties of Fe/Mn deposits were recovered:

[14] 1. Yellow-brown to black Fe-Mn encrustations that occur on hard rock substrates (Figure 1) are friable, layered or laminated and have predominantly botryoidal or granular to smooth surfaces. These deposits are referred to as Fe-Mn crusts (Figure 2a).

[15] 2. Brown, gray, and black Mn (more rarely Fe) oxides that cement volcaniclastic sandstone, breccia, and

conglomerate (Figure 2b) are generally earthy and friable and are submetallic gray in some samples. These deposits are referred to as Mn sandstone.

[16] 3. Pale to dark gray, rarely brownish gray, Mn oxides occur as stratiform, stratabound layers with a submetallic to metallic (rarely glassy) luster (Figures 2c and 2d). These deposits form discrete beds and lenses millimeters to centimeters thick within sandstone and Mn-cemented sandstone. The Mn oxides are friable to dense, massive to laminated, and brittle. Pebble- and cobble-sized chunks of these beds were recovered in several dredge hauls with only minor amounts of the host sandstone, which was lost during dredging. These deposits are referred to as stratabound Mn, although it should be noted that the Mn sandstone is also a stratabound deposit.

[17] 4. Dark gray, submetallic, irregularly shaped masses of Mn were recovered in dredge hauls D3, D20, and D28 (Figure 2e). These deposits are compositionally (see section 4.2) similar to the stratabound Mn but differ in texture, irregular morphology, and host sediment. A small amount of ocher to red mud was collected with these samples.

[18] 5. Two cobbles composed of magnetite, goethite, and siderite were recovered from the submerged caldera of Maug volcano in dredge D12. Fresh surfaces of these black cobbles exposed to air altered within days to yellow-brown goethite, reflecting the fine-grain size of the hydrothermal magnetite.

[19] In summary, the Fe-Mn crusts and Mn sandstones are mixed Fe-Mn deposits, whereas the stratabound Mn contains little Fe and the magnetite/siderite deposit little Mn.

4.1. Sample Textures

4.1.1. Macroscopic Textures

[20] The two types of stratabound deposits, Mn sandstone and stratabound Mn, contain variable amounts of detritus and form a continuum between the end-members. The dense stratabound Mn layers occur within both Mn sandstone beds and otherwise unmineralized sedimentary rocks. The two types of stratabound deposits display several textures: (1) evenly distributed uniform cement, (2) fingers or dendrites of Mn oxide cement oriented perpendicular to the bedding, with friable sediment between the dendrites, (3) dense layers and lenses within sandstone and breccia, and (4) fracture and vug fill within breccia.

[21] The lower surface of stratabound Mn layers is commonly botryoidal and smooth with a polished, metallic to submetallic appearance. These layers formed along preferred stratigraphic intervals, such as bedding planes, fractures parallel to bedding, and intervals of textural contrast.

[22] Dredges 3, 20, and 28 recovered stratabound Mn of irregular shapes, without associated sediment (Figure 2c). These stratabound layers consist of intercalated dense Mn oxides and fibrous porous Mn oxides; both are associated with X-ray amorphous, iron-rich, ocher to reddish muds, presumably of hydrothermal origin. Muds of hydrothermal origin were also recovered with stratabound Mn oxides elsewhere in the IBM arc [*Usui and Nishimura*, 1992a, 1992b].

4.1.2. Microscopic Textures

[23] Textural diversity was determined from the study of 27 doubly polished thin sections and includes botryoidal laminae, homogeneous dense layers, laminated dense layers, porous fibrous laminae, and scalloped textures. Within those textures, we define three mineral-size classes, with decreasing size: crystallites, microcrystallites, and amorphous cryptocrystalline (AC) oxides; these are similar to textures described by *Kang and Kosakevitch* [1984] for hydrothermal samples from the Lesser Antilles volcanic arc. Crystallites are acicular needles of Mn oxides up to 500 μm long and occur in three forms: Layers of aligned crystallites, mosaics of crystallites, and radially oriented crystallites (Figures 3a and 3b). Microcrystalline Mn oxide is finely crystalline and does not occur in characteristic forms (Figure 3c). AC Mn oxides are isotropic in polarized reflected light and distinguishable by differential relief in plane light (Figure 3c). These oxides appear softer and usually have lower relief than microcrystallites and crystallites (Figure 3d). AC oxides have no discernible crystal structure and are probably X-ray amorphous but are too small to isolate for XRD analysis.

[24] Botryoidal textures commonly coalesce into layers and can be densely packed or have pore space between botryoids. Individual botryoids are composed of alternating laminae of aligned crystallites, microcrystallites, and AC Mn oxides. Homogeneous layers are generally microcrystalline, whereas laminated textures are generally composed of intercalated microcrystalline and crystalline laminae. Porous, fibrous Mn oxides consist of long fibers that are commonly subparallel and rarely dendritic (Figure 3e). Porous fibrous Mn oxide on a sample surface produces a velvety appearance. In thin section, porous, fibrous oxides are generally AC oxides, although microcrystalline fibers also exist. Scalloped Mn oxides consist of scales of radially oriented crystallites (Figure 3f).

[25] SEM images show that porous, fibrous Mn oxides from a fracture surface of sample D3-3 are composed of subparallel fibers with irregular surfaces (Figure 4a). Broken fibers show a homogeneous internal structure. In contrast, botryoids are composed of layers of aligned crystallites (Figure 4b). A fracture surface of sample D44-4 shows botryoidal Mn oxides overlain by radially oriented crystallites (Figure 4c); this secondary electron image shows the crystallites and the open network of an outer surface of aligned crystallites (upper left of center). A backscatter electron image (not shown) of D44-4 shows that intercalated AC oxides and microcrystalline oxides occur within the botryoidal structure and that the AC oxides contain much higher water contents than the microcrystalline oxides.

[26] AC oxides form the cores of radially oriented crystallites (Figure 4d) and are intercalated with microcrystallites or crystallites in botryoidal and laminated structures (Figures 4e and 4f). In backscattered images, crystallites have a higher mean atomic number (brighter) than the AC oxides, which we interpret to reflect lower water contents in the crystallites, consistent with the SEM-EDX and electron microprobe results. In most samples, AC oxides appear to be the initial phase of deposition and further precipitation of Mn oxides proceeded outward from AC cores and layers. It is likely that the AC Mn oxides formed by rapid oxidation and precipitation on mixing of mineralizing fluids with oxygenated pore waters. This rapid precipitation may have been bacterially mediated/accelerated as it is in oxygenated hydrothermal plumes [*Cowen et al.*, 1986, 1990]. The

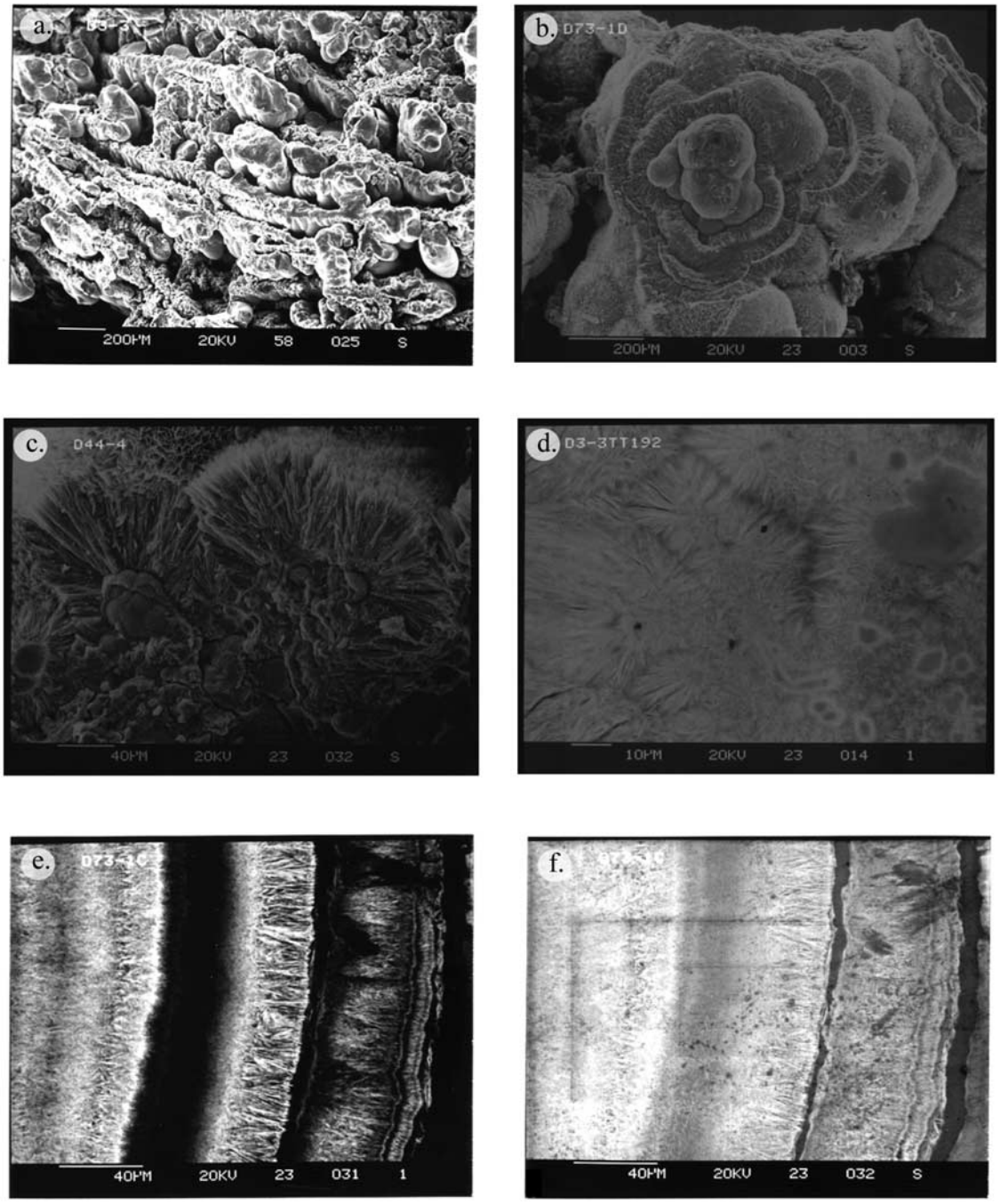

Figure 4. SEM photomicrographs: (a) fibrous porous Mn oxides from a fracture surface, D3-3; (b) botryoidal/colloform Mn oxides from a fracture surface, D73-1D; (c) radially oriented crystallites above botryoidal/colloform laminated Mn oxides from a fracture surface, D44-4; (d) backscatter electron image of crystallites radiating from AC cores; the AC cores have higher water contents, and therefore are darker in the image, D3-3; (e) and (f) backscatter electron and secondary electron images, respectively, showing alternating laminae of aligned crystallites and AC oxides, D73-1C; in the backscatter image, the AC layer is nearly black because of high water contents.

crystalline and microcrystalline Mn oxides reflect slower reaction kinetics due to less oxygenated pore fluids, less Mn enrichment in the fluids, or longer time intervals over which precipitation took place. The waxing and waning of mineralizing fluids (hydrothermal pulses) interacting with oxygenated pore fluids can explain the occurrence of intercalated AC oxides (rapid precipitation, waxing stage), microcrystallites, and crystallites (slower precipitation, waning stages) within the botryoidal and laminated Mn oxides (Figures 4e and 4f); as well as the alternating massive (rapid precipitation, waxing stage) and porous-fibrous layers (slower precipitation, waning stage; Figure 3d).

Table 3. Electron Microprobe Spot Analyses of Crystalline and Microcrystalline Mn Oxides[a]

	Na	Mg	Si	S	Ca	Ti	Mn	Fe	Ni	Cu	Mo	Ba	Pb
D3-3A	1.80	0.19	-	-	0.26	0.01	22.2	0.02	0.01	-	0.01	-	0.04
D3-3B	1.91	0.25	-	0.03	0.29	-	24.3	0.05	0.01	-	0.02	0.01	0.03
D3-3C	1.94	0.25	-	0.01	0.30	-	24.5	0.04	-	-	0.03	0.02	-
D3-3D	1.86	0.26	-	-	0.28	-	25.3	0.04	0.02	-	0.01	-	0.03
D3-3E	2.14	0.34	-	0.02	0.32	-	27.7	0.04	-	-	0.03	0.02	0.04
D3-3H1	1.78	0.21	-	0.02	0.26	-	22.0	0.02	-	-	0.05	-	0.07
D3-3H2	1.80	0.20	-	0.03	0.26	-	21.8	0.02	0.02	-	0.03	-	-
D3-3H3	1.92	0.25	-	-	0.29	-	24.8	0.04	0.02	-	0.01	-	0.07
D3-3H4	1.91	0.24	-	0.02	0.28	0.01	24.6	0.04	-	0.02	0.02	0.01	-
D3-3H5	1.91	0.24	-	0.01	0.28	-	24.5	0.05	0.04	-	0.05	0.03	0.09
D3-3H6	1.84	0.21	-	0.01	0.28	0.02	23.3	0.04	-	-	0.02	-	-
D3-3H7	1.80	0.16	-	0.02	0.23	0.01	21.7	0.04	0.02	-	-	0.01	-
D3-3H8	2.02	0.26	-	0.06	0.29	0.01	25.2	0.01	0.02	-	0.01	-	0.13
D3-3G1	2.14	0.65	-	0.04	0.34	0.01	45.6	0.09	0.01	-	0.06	0.17	0.01
D3-3G3	2.76	0.59	-	0.09	0.34	0.01	46.2	0.09	0.04	0.05	0.14	0.10	0.05
D3-3G4	3.14	0.54	-	0.04	0.37	-	47.1	0.09	0.03	0.04	0.08	0.07	0.01
D3-3G6	3.20	0.49	-	0.09	0.35	-	47.5	0.09	0.01	0.05	0.09	0.09	0.04
D3-3G7	2.95	0.53	-	0.07	0.38	-	47.1	0.09	0.03	0.04	0.10	0.06	0.01
D3-3G8	3.09	0.60	-	0.05	0.38	0.006	47.1	0.10	0.04	0.04	0.13	0.09	0.05
D3-3G9	3.18	0.13	-	-	0.17	-	31.8	0.03	-	-	0.06	0.02	-
D3-3I	1.14	0.57	0.43	0.21	0.34	-	38.6	0.10	0.04	-	0.10	0.32	0.10
D8-12A	1.42	3.11	0.58	0.10	0.28	0.042	30.9	0.12	-	-	0.02	0.07	0.04
D8-12B	1.42	2.78	0.57	0.08	0.30	0.050	31.3	0.26	0.04	-	0.02	0.07	0.09
D812-2	0.99	3.52	0.79	0.21	0.27	0.07	29.5	0.30	0.02	-	0.02	0.03	0.07
D812-5	1.74	3.11	0.32	0.05	0.37	0.03	37.8	0.09	0.02	-	0.02	0.10	0.12
D812-5	1.90	2.72	0.45	0.08	0.37	0.04	37.8	0.11	-	-	0.05	0.14	0.05
D812-5	1.68	2.90	0.72	0.06	0.33	0.02	37.4	0.10	0.05	-	0.01	0.08	-
D812-6	1.50	3.15	0.85	0.05	0.30	0.09	34.3	0.22	-	-	0.02	0.37	0.14
D812-6	1.89	3.24	1.65	0.14	0.33	0.16	36.2	0.35	0.08	-	0.03	0.39	0.26
D812-6	1.60	3.25	1.25	0.13	0.33	0.18	38.5	0.27	-	-	0.01	0.83	0.20
D812-8	1.37	3.20	0.65	0.27	0.26	0.03	30.9	0.10	0.01	-	0.01	0.03	0.10
D812-8	1.61	3.64	0.57	0.11	0.30	0.07	35.0	0.13	0.01	0.03	0.01	0.05	0.13
D812-8	1.35	3.26	0.65	0.20	0.27	0.07	31.9	0.11	0.01	-	0.02	0.09	0.01
D812-9	1.48	3.03	0.45	0.11	0.28	0.06	32.6	0.07	0.03	-	0.01	0.08	-
D812-9	1.73	3.31	0.48	0.11	0.29	0.05	34.6	0.09	0.04	-	0.02	0.05	0.05
D812-9	2.05	3.14	0.54	0.16	0.35	0.04	38.5	0.11	-	0.01	0.03	0.12	0.08
D812-10	1.74	3.20	1.09	0.21	0.32	0.05	35.2	0.13	0.03	0.01	0.01	0.06	-
D812-10	1.83	3.11	0.82	0.25	0.36	0.09	34.7	0.14	0.01	0.04	0.01	0.06	0.16
D812-10	1.62	2.95	1.32	0.18	0.32	0.16	31.5	0.37	0.07	-	0.01	0.07	0.05
D812-11	1.67	3.35	0.59	0.20	0.33	0.15	35.3	0.15	0.04	-	-	0.10	0.09
D812-11	1.40	3.44	1.06	0.18	0.31	0.18	33.2	0.15	0.03	0.03	0.03	0.06	0.05
D812-11	1.48	3.20	0.81	0.11	0.31	0.16	33.3	0.35	-	-	-	0.03	0.06
D812-12	1.66	3.35	0.92	0.18	0.32	0.17	33.5	0.11	-	-	0.02	0.10	0.13
D812-12	1.66	3.47	0.94	0.07	0.34	0.13	34.2	0.14	0.01	-	0.01	0.06	0.04
D812-12	1.50	3.31	1.55	0.17	0.34	0.11	34.7	0.16	0.00	-	0.01	0.10	-
D73-1C1	2.20	2.21	-	0.02	0.34	0.04	39.2	0.11	0.01	-	0.01	0.15	0.04
D731C3	1.67	2.32	0.45	0.03	0.77	0.04	37.1	0.31	0.04	0.02	0.02	0.31	0.02
D731C-4	1.68	3.05	0.28	0.06	0.41	0.07	38.3	0.33	0.04	-	0.03	0.39	0.02
D73-1C5A	1.11	3.34	5.00	0.09	0.54	0.29	26.4	3.47	0.08	0.05	-	0.33	-
D73-1C5B	0.70	3.56	1.99	0.033	0.27	0.567	25.9	2.83	0.14	0.03	0.01	0.22	-
D73-1CC	1.63	2.63	0.03	0.014	0.25	0.11	42.4	0.37	0.07	0.05	0.03	0.46	0.01
D73-1C5D	1.46	2.58	0.49	0.101	0.27	0.10	42.5	0.44	0.05	0.01	0.03	0.44	0.17
D73-1C5E	1.56	2.80	-	0.039	0.26	0.033	42.2	0.15	-	0.01	0.02	0.64	0.02
D73-1C6	2.00	2.71	0.49	0.08	0.20	0.062	40.9	0.41	0.04	0.03	0.02	0.66	0.10
D73-1C7	2.09	2.59	0.58	0.012	0.20	0.11	40.9	0.56	0.05	0.01	0.03	0.45	0.10
D73-1C8	1.96	3.00	0.75	0.068	0.21	0.056	41.0	0.28	0.02	0.01	0.01	0.36	0.04
D731C-9	1.51	3.02	0.73	0.042	0.20	0.158	34.4	0.39	-	0.02	0.04	0.35	0.04
D731C-10	1.94	2.38	0.39	0.024	0.23	0.089	42.6	0.25	0.03	-	0.05	0.37	-
D73-1C-11	1.90	3.02	0.62	0.032	0.24	0.099	39.1	0.39	0.03	0.03	0.01	0.34	0.02
D73-1C-12	2.12	3.14	0.30	0.127	0.26	0.094	40.4	0.38	0.01	0.02	0.02	0.26	0.10
D73-1C-13	1.91	2.97	0.43	0.102	0.28	-	41.1	0.10	0.02	0.01	0.01	0.23	-
D73-1C-14	2.45	2.03	0.29	0.091	0.38	-	44.1	0.17	0.01	-	0.03	0.22	0.07
D73-1C-15	2.25	1.62	-	0.078	0.35	-	39.2	0.17	0.02	0.02	0.02	0.07	0.01
D73-1C-16	2.51	1.49	-	0.016	0.28	-	35.5	0.10	0.02	-	0.02	0.02	0.08
Average	1.86	2.10	<0.80	0.09	0.31	<0.09	34.7	0.26	<0.03	<0.03	<0.03	<0.18	<0.07
Maximum	3.20	3.64	5.00	0.27	0.77	0.57	47.5	3.47	0.14	0.05	0.14	0.83	0.26
Minimum	0.70	0.13	<0.01	<0.01	0.17	<0.01	21.7	0.01	<0.01	<0.01	<0.01	<0.01	<0.01
SD	0.50	1.30	0.79	0.07	0.08	0.09	7.3	0.54	0.02	0.02	0.03	0.19	0.05

[a]Values in weight %. Dash indicates below the limit of detection.

Table 4. Electron Microprobe Spot Analyses of Amorphous (AC) Mn Oxides[a]

	Na	Mg	Si	S	Ca	Ti	Mn	Fe	Ni	Cu	Mo	Ba	Pb
D3-3G2	0.67	0.24	-	0.01	0.07	-	16.39	-	0.04	-	0.01	0.02	-
D8-12C	0.62	1.97	0.38	0.03	0.14	0.05	15.61	0.11	0.01	-	-	0.01	0.04
D8-12D	0.65	1.78	0.42	0.04	0.16	0.07	16.60	0.59	-	-	-	-	0.05
D8-12E	0.50	1.74	0.73	0.01	0.12	0.20	14.00	0.77	-	-	0.01	0.05	0.01
D812E2	0.50	1.61	0.60	0.02	0.12	0.25	14.14	0.60	-	-	0.01	0.09	0.04
D812-7	0.33	1.30	0.22	0.04	0.07	0.04	10.34	0.09	-	-	0.01	-	0.04
D812-7	0.29	1.21	0.31	0.02	0.08	0.06	9.49	0.14	-	-	-	-	-
D812-7	0.42	1.56	0.25	0.03	0.09	0.03	12.17	0.11	0.02	-	-	-	-
D812-13	0.40	1.71	0.25	0.01	0.11	0.05	13.29	0.15	-	-	-	-	0.01
D812-13	0.43	1.94	0.30	0.01	0.12	0.05	15.61	0.25	-	-	0.01	0.01	0.02
D812-13	0.39	1.62	0.25	-	0.12	0.05	13.78	0.37	-	-	-	-	-
D73-1C2	0.82	3.64	3.45	0.04	0.09	0.38	14.14	2.28	0.09	0.11	0.01	0.05	0.07
Average	0.50	1.69	0.65	0.02	0.11	0.11	13.80	0.50	<0.04	<0.11	<0.01	<0.04	<0.03
Maximum	0.82	3.64	3.45	0.04	0.16	0.38	16.60	2.28	0.09	0.11	0.01	0.09	0.07
Minimum	0.29	0.24	0.22	0.01	0.07	0.03	9.49	0.09	<0.01	<0.11	<0.01	<0.01	<0.01
SD	0.16	0.77	0.94	0.01	0.03	0.11	2.23	0.64	0.04	-	-	0.03	0.02

[a]Values in weight %. Dash indicates below limit of detection.

4.1.3. Electron Microprobe Composition of Microtextures

[27] The microprobe was used to evaluate compositional differences among the crystalline and AC manganates. The stratabound Mn sample D3-3 and two Mn sandstone samples (D73-1 and D8-12) were analyzed because they display a variety of textures. Sample D73-1C contains both volcaniclastic and foraminiferal sandstones and D8-12 has a thin stratabound Mn layer within the sandstone.

[28] Electron microprobe analyses caused pitting in the AC oxides even at a low current of 15 nA. Pitting by the electron beam is indicative of degassing. An attempt to degas the Mn oxides by leaving the thin sections in the vacuum of the microprobe overnight had little effect. Microcrystalline oxides showed evidence of minor pitting, but not as extensive as the AC oxides; the crystallites rarely pitted. The volatile burn off caused element totals to be low. The high loss on ignition (LOI) and H_2O contents (Table 2) verify high contents of volatiles. When microprobe elements are summed using their most oxidized forms and normalized to 100% on a water-free basis, the normalized Mn contents of the AC and crystalline oxides are roughly the same.

[29] Sample D3-3 has Si concentrations below the microprobe detection limit, whereas samples D73-1C and D8-12 have low but measurable Si (Tables 3 and 4). AC oxides have somewhat higher mean concentrations of Ti, Fe, and Ni than the crystalline oxides; however, abundances are still generally under 1%. The remaining elements are enriched in the crystalline oxides. The characteristic difference is that Mn in the crystalline oxides ranges from 22% to 47% whereas in the AC oxides Mn ranges from 9% to 17% (Tables 3 and 4). This large difference reflects the greater water contents and smaller particle sizes of the AC phase. Small particle size results in higher porosity and charge imbalances, which create a greater capacity for water adsorption. Areas of high porosity and hydrous minerals create lower total counts on the microprobe and therefore lower measured Mn in the AC Mn oxides.

[30] Plots of Mg, Ca, and Na against Mn show that, in general, these elements increase with increasing crystallinity (Figure 5). D3-3 crystalline oxides always plot in two

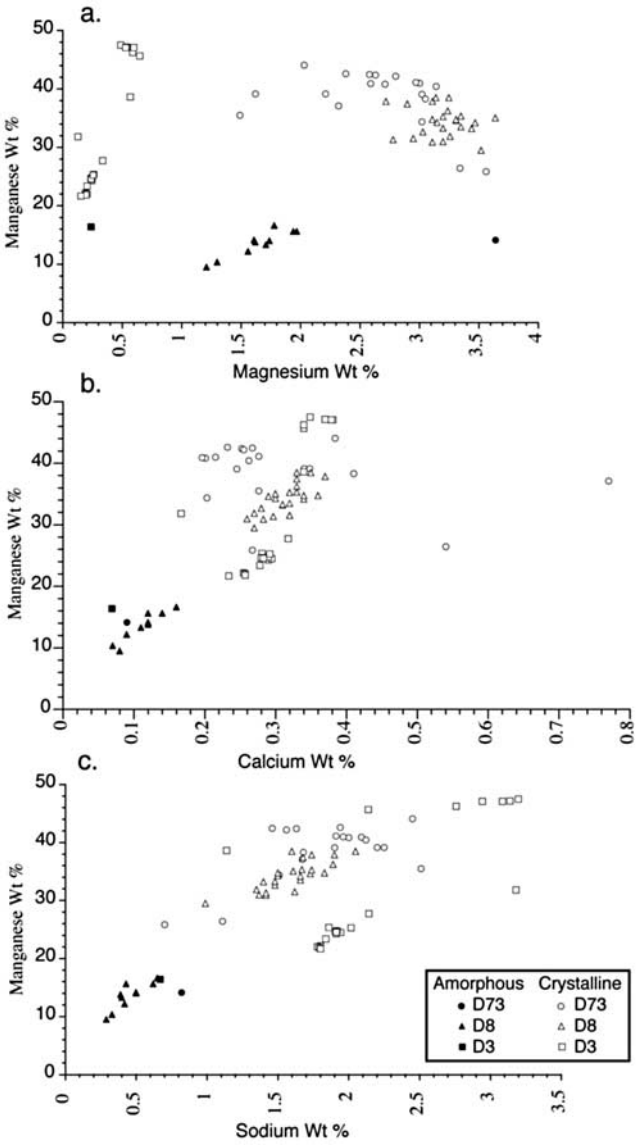

Figure 5. Scatterplots of (a) Mg, (b) Ca, and (c) Na versus Mn from electron microprobe spot analyses of amorphous cryptocrystalline Mn oxides and crystalline Mn oxides in three samples.

Table 5. Statistics for 28 Mn-Sandstone and Mn-Breccia Samples, Group 1; 12 Mn-Sandstone and Mn-Breccia Samples, Subgroup 2A; and 21 Stratabound Mn Samples, Subgroup 2B[a]

	Mn-Sandstone and Mn-Breccia Samples																	
	Group 1						Subgroup 2A						Stratabound Mn Samples, Subgroup 2B					
	N	Mean	Median	SD	Min	Max	N	Mean	Median	SD	Min	Max	N	Mean	Median	SD	Min	Max
Fe	28	8.39	6.34	5.21	4.00	26.5	12	4.23	3.90	1.83	1.67	6.80	21	0.888	0.526	1.09	0.081	4.69
Mn	28	12.4	12.6	4.37	4.50	20.9	12	33.7	35.3	4.72	26.9	41.0	21	47.5	48.0	2.56	41.9	50.8
Fe/Mn	28	0.749	0.615	0.471	0.284	2.08	12	0.127	0.116	0.056	0.057	0.220	21	0.020	0.011	0.025	0.002	0.107
Si	27	17.0	17.3	3.75	6.71	24.8	12	7.72	7.32	1.87	5.23	10.6	21	1.17	1.12	1.05	0.051	4.15
Na	27	2.09	2.18	0.406	1.06	2.74	12	2.62	2.45	0.673	1.82	3.93	21	2.57	2.48	0.660	1.46	3.81
Al	28	5.86	6.15	2.13	0.406	8.78	12	2.45	2.52	1.45	0.107	4.82	21	0.550	0.495	0.396	0.115	1.49
Mg	28	2.10	2.13	1.22	0.364	6.70	12	2.02	2.03	0.687	1.18	3.64	21	1.93	2.07	0.651	0.526	2.95
Ca	28	4.82	4.93	1.85	0.988	8.70	12	2.86	2.14	1.81	1.34	7.97	21	1.74	1.73	0.357	1.03	2.43
K	28	0.925	0.861	0.407	0.364	2.09	12	1.22	1.10	0.404	0.762	1.94	21	1.03	1.05	0.396	0.325	1.75
Ti	28	0.379	0.364	0.172	0.061	0.917	12	0.146	0.135	0.082	0.047	0.346	21(3)	~0.039	~0.030	~0.030	<0.01	0.101
P	28(1)	~0.109	~0.092	~0.079	<0.025	0.315	12(3)	~0.069	~0.069	~0.045	<0.025	0.171	21(7)	~0.068	~0.045	~0.057	<0.025	0.206
H_2O^-	28	3.17	2.60	1.81	1.20	9.20	12	5.57	5.65	2.06	2.70	9.40	21	7.28	7.00	3.38	3.00	20.1
H_2O^+	27	4.01	3.60	2.14	0.980	10.1	12	6.54	6.40	0.896	5.46	8.28	21	8.91	8.98	1.15	7.12	11.2
CO_2	27	0.327	0.083	0.638	0.010	3.21	12	0.681	0.042	1.77	0.011	6.11	21	0.109	0.065	0.154	0.021	0.724
LOI	10	10.03	8.22	5.25	4.66	19.2	3	20.1	20.2	0.208	19.9	20.3	13	24.5	24.3	3.31	20.3	34.0
As	23(1)	~81.6	~19.4	~177	<2	850	11	48.2	48.6	24.6	20.7	105	21	68.0	52.3	33.5	29.2	147
Ba	24	977	815	759	233	2960	11	1236	1071	507	596	2301	21	1508	972	1386	464	5319
Cd	24(1)	~6.16	~5.30	~5.97	<0.1	22.6	11(3)	~6.42	~6.06	~5.55	<0.1	18.6	21	23.5	14.3	25.1	0.522	86.1
Co	24(1)	~226	~54.0	~332	<5	1169	11	123	91.0	95.6	12.4	293	21(3[b])	~72.7	~36.3	~111	3.37	501
Cr	24	34.6	21.8	33.9	5.95	142	11	5.38	4.14	4.59	1.60	15.5	21(7)	~2.49	~2.47	~1.88	<1	7.24
Cu	24	419	200	811	46.2	4107	11	144	70.1	129	45.5	441	21	280	128	317	16.3	983
Mo	24(3)	~147	~86.4	~170	<5	804	11	476	504	232	104	763	21	651	548	314	252	1363
Ni	24	330	236	359	21.4	1437	11	185	183	69.4	75.6	299	21	349	215	310	31.3	1026
Pb	24(14)	~87.3	~37.5	~151	<10	682	11(3[b])	~35.7	~37.5	~14.1	16.0	65.2	21(8)	~69.5	~37.5	~53.5	<10	162
Sr	24	503	435	206	213	1049	11	508	546	143	287	732	21	564	545	168	371	1145
V	24	274	250	118	72.7	609	11(4)	~108	~59.6	~185	<5	639	21(4)	~232	~260	~211	<5	819
Y	24	37.3	25.7	32.3	13.2	136	11	11.3	10.7	2.62	7.73	16.4	21(6[b])	~17.8	~18.1	~15.1	3.14	64.0
Zn	24	~286	~282	~148	84.0	588	11(1[b])	~138	~150	~65.2	37.3	216	21	3058	458	4319	18.8	13109
Hg	6(4)	~17	~15	~2.7	<20	20	0	–	–	–	–	–	7(4)	~18	~15	~5.3	<15	29
Pd	12	3.2	2.6	1.2	2.0	5.7	4	1.9	1.7	0.81	1.3	3.0	5(1[b])	~6.4	~7.0	~6.0	1.0	16
Pt	12(1)	~19	~7.7	~24	<5	88	4(2)	~7.9	~7.0	~5.0	<5	14	5(2)	~18	~8.5	~22	<5	56
Rh	12(12)	-	-	-	-	-	4(4)	-	-	-	-	-	7(5)	~10	~0.75	~17	<1	41
Depth (m)	28	1683	1529	517	885	2540	12	1231	1126	568	114	1880	21	1590	1533	671	876	2918
Thickness (mm)	26	26	20	21	5	90	12	28	27	17	1	60	21	15	12	12	2	40

[a]Statistics calculated using hygroscopic water-free data as reported in Table 2. N in parentheses indicates number of samples with below detection limit values; for those samples statistics were calculated using 0.75X (detection limit); the minimum value stated here is the detection limit itself. Major elements are in percent (or weight percent), minor elements are in ppm, and Hg and platinum group elements are in ppb.
[b]The minimum value reported is an actual value lower than the detection limit for other samples.

groups; the microcrystalline oxides are lower in Mn and generally lower in Ca, Mg, and Na than the crystallite oxides. The highest Na values are from the crystallites of D3-3. The high Na/Mn ratios for all D3-3 Mn oxides may indicate seawater-mineral exchange.

[31] A plot of Mg versus Mn (Figure 5a) shows that D3-3 is lower in Mg than the other two samples. Generally, low Mg is indicative of a proximal subseafloor hydrothermal deposit because it is removed readily from hydrothermal fluids during alteration of arc rocks creating Mg silicates (usually clay minerals). Mg is enriched in more distal deposits when hydrothermal fluids mix with pore fluids and seawater [*Mottl*, 1983]. Sample D3-3 may therefore have formed closer to the source of the hydrothermal fluids than either D8-12 or D73-1C.

[32] In general, the plot of Ca versus Mn (Figure 5b) shows a similar trend of increasing concentrations with increasing crystallinity. D73-1C has two anomalously high Ca values that were taken in a Mn oxide cemented foraminifera-rich sandstone and may reflect the dissolution of tests as a source of the high Ca, which was then adsorbed onto the Mn oxides.

[33] Na, Mg, and Ca concentrations may be indicators of differing conditions during Mn oxide mineralization. Low Mg contents may reflect precipitation proximal to the hydrothermal source, whereas high Na may indicate seafloor or near seafloor deposition. High Ca values probably reflect a carbonate sediment source. Alternatively, high Na, Mg, and Ca may reflect adsorption during postdepositional exposure at the seabed.

4.2. Mineralogy of Manganese Oxides

[34] Mn oxide minerals found in Mariana samples include 10 Å (todorokite and/or buserite) and 7 Å (birnessite) manganates, and possibly also vernadite (δ-MnO_2). Todorokite and buserite have similar X-ray diffraction reflections and XRD alone cannot differentiate between them [*Burns and Burns*, 1977]. Vernadite is defined by only two X-ray reflections at about 2.4 Å and 1.4 Å. Birnessite has two additional reflections to those found in vernadite at about 7.2 Å and 3.5 Å, whereas the 10 Å phase has two additional reflections to those found in vernadite at about 9.6 Å and 4.8 Å. In several Mariana samples, the 10 Å phase also has a reflection at about 3.4 Å, which is not commonly found in modern marine Mn deposits but does occur in on-land Mn deposits containing todorokite/buserite. Vernadite is difficult to identify when accompanied by the 10 Å and/or 7 Å manganates because of the overlapping reflections and must be inferred to occur if the relative intensities of the 2.4 Å and 1.4 Å reflections appear anomalous, which was rarely the case in Mariana samples. Recent work indicates that the phyllomanganates have no significant structural differences and therefore the 10 Å buserite, 7 Å birnessite, and vernadite are structurally the same and by way of precedence in nomenclature should all be called vernadite, such as 10 Å vernadite, 7 Å vernadite, and vernadite, respectively [*Manceau et al.*, 2007]. We will use the general designations of 10 Å and 7 Å manganates, and vernadite. For Mariana samples, Fe-Mn crusts consist solely of vernadite, with rare exceptions of minor 10 Å or 7 Å manganates. Stratabound Mn deposits consist predominantly of 10 Å and 7 Å manganates.

[35] Two types of 10 Å manganates exist in the Mariana samples: A mineral that collapses to 7 Å manganate through dehydration and oxidation when exposed to air (e.g., sample D3-8); and a manganate that does not collapse after drying (e.g., D3-1). Most samples seem to be a mixture of these two 10 Å manganates. We consider the 7 Å manganate in our samples to be predominantly a transformation product created by collapse of a structurally unstable 10 Å manganate, whether or not the original 10 Å phase was identified by XRD [see also *Usui et al.*, 1989]. When todorokite tunnels have walls of greater than three chains long, they are structurally unstable. Without stabilizing cations, absorbed water, or formation at a relatively higher temperature, the tunnel structure collapses to a 7 Å phase [*Usui et al.*, 1989; *Mellin and Lei*, 1993].

[36] In the IBM samples, the 10 Å manganate presumably collapsed completely to a 7 Å manganate in six samples, although samples D3-3I and D3-8 are the only two that were X-rayed quickly enough after exposure in air to document this transformation. Consequently, we cannot rule out the possibility that a primary 7 Å manganate was present in some samples [see *Ostwald and Dubrawski*, 1987]. We documented the complete collapse of a 10 Å manganate to a 7 Å manganate that took place in less than two weeks in sample D3-8. This sample was stored in water after collection, ground while wet, and air-dried for about 2 h before being X-rayed the first time. The sample was then kept at room temperature for two weeks and X-rayed again. The transformation from a well crystallized 10 Å manganate to a moderately well crystallized 7 Å manganate was complete. The 10 Å manganate remained stable in 17 samples, completely collapsed in six samples as mentioned above, and only partially collapsed to a 7 Å phase in the remaining 34 samples.

4.3. Crystallinity of Manganese Oxides

[37] Changes in crystallinity associated with the transformation of 10 Å to 7 Å manganate were determined by reanalyzing samples after intervals ranging from 2 weeks to 2 years. Crystallinity (peak height/peak width at half height) of the Mn oxide minerals is highly variable with reflections ranging from broad low-intensity to sharp high-intensity peaks for each mineral. Crystallinity increases with increasing exposure to air in most samples of noncollapsing 10 Å manganate and for the 7 Å manganates if present in the initial scan. Increases in 7 Å manganate crystallinity can be accompanied by either a decrease or an increase in the accompanying 10 Å manganate crystallinity.

[38] Changes in crystallinity are the result of dehydration through loss of both absorbed and structural water, and perhaps also through oxidation. The increased crystallinity of the stable 10 Å manganate probably reflects dehydration, which results in decreased distortion of the tunnel structure; a few 10 Å manganate samples did not increase in crystallinity with time. The crystallinity of the 7 Å manganate continued to increase with time because the 10 Å to 7 Å transformation proceeded with continued dehydration and oxidation.

[39] The transformation of the 10 Å manganate to 7 Å manganate does not appear to be related to deposit type, texture, age of the Mn oxide deposit, or composition of the sandstone. On the basis of the spatial distribution of Mn

minerals in hydrothermal Mn deposits from Kaikata Seamount (Izu-Bonin arc), *Usui et al.* [1989] proposed that higher temperatures of mineralization produced more stable 10 Å phases, that is with closer proximity to the hydrothermal source. We suggest that a similar mechanism was responsible for the stability of the 10 Å manganates collected by dredging in this study. If this is correct, then some of the samples from dredge hauls D3, D8, D15, D28, D57, and D73, and all samples from D13, D47, and D54 formed from higher temperature mineralizing fluids than the other samples. However, dredging recovers samples from a rather large area and some dredge hauls contained both non-collapsible and fully collapsible 10 Å manganates. The least stable, lowest temperature 10 Å manganates were found in dredge hauls D3, D41, D52, and D55.

4.4. Chemical Composition

[40] Samples were grouped in order to calculate mean compositional data and for statistical analyses, including correlation coefficient matrices and Q-mode factor analyses: Group 1, stratabound grain-supported, Mn-cemented sandstones with 4–21% Mn; and Group 2, stratabound Mn with 27–51% Mn (Table 5). This division is based on a break in Mn concentrations of five percentage points, otherwise the Mn concentrations form a near continuum within each group. Group 2 samples were further subdivided into Subgroup 2A samples with 27–41% Mn, and Subgroup 2B with >41% Mn. This subdivision is based on the occurrence of macroscopically identifiable detrital grains in Subgroup 2A samples, which generally show cement-supported textures, unlike Group 1 Mn sandstones; Subgroup 2B samples do not contain macroscopically identifiable detrital grains and comprise the nearly pure hydrothermal Mn end-member. Analyses of Mn sandstones (Group 1; Subgroup 2A) were completed on bulk samples; the composition therefore reflects the framework/cement ratio and the framework grain composition in addition to the Mn mineralization (Tables 2 and 5). Analyses of stratabound Mn (Subgroup 2B) include layers removed from their sandstone and breccia hosts and deposits collected without host material. Analyses of two unusual magnetite-goethite-siderite samples are also presented (Table 2).

[41] Fe/Mn ratios for Group 1 Mn sandstone samples average 0.75, whereas the mean for Group 2 Mn sandstone and stratabound Mn samples is significantly lower, 0.06. Fe, Fe/Mn, Si, Al, Ca, Ti, Co, and Cr decrease from Group 1 through Subgroup 2A to Subgroup 2B samples, whereas Mn, Ba, Cd, Mo, and volatiles (H_2O^-, H_2O^+, LOI) show the opposite trend. Subgroup 2B (high Mn) samples are also highest in Ni and Zn. Only CO_2 is highest in Subgroup 2A samples, whereas As, Cu, Ni, Pb, Pt, V, Y, and Zn are lowest in Subgroup 2A samples and higher in both Group 1 and Subgroup 2B samples. Mg, K, and Sr have about the same concentrations in Group 1 and Subgroups 2A and 2B samples. P and Na concentrations increase from Group 1 to Group 2 samples. These trends reflect the higher aluminosilicate fraction (Si, Al, Ca, Ti, Cr) in Group 1 samples, higher biocarbonate (CO_2 and part of the Ca) and biosilica (Si/Al ratios) in Subgroup 2A samples, and higher hydrothermal component (Mn, Ba, Cd, Mo, Ni, Zn) in Subgroup 2B samples. The increasing water contents with increasing Mn reflect water (up to 20 wt % H_2O^-) adsorbed by the Mn oxide minerals and incorporated into their structural framework at the time of formation (up to 11 wt % H_2O^+).

[42] Group 1 samples have more As and Ni than Subgroup 2A samples, indicating that a component of these two elements is probably associated with the aluminosilicate fraction. Mean Cd contents are about the same in Group 1 and Subgroup 2A samples, indicating that it is enriched only in the most Mn-rich samples (Subgroup 2B).

[43] High Li [*Chan and Hein*, 2007], Mo [*Kuhn et al.*, 2003], and Cd [*Moorby et al.*, 1984] contents determined here and in other Mn deposits are indicators of a hydrothermal origin, but their wide ranges of concentrations caution that these proxies need to be combined with supporting evidence. Li is perhaps the element most consistently high in hydrothermal Mn deposits, being typically 1–3 orders of magnitude higher than Li contents in hydrogenetic Mn deposits. Zn is also very high in some hydrothermal Mn samples (i.e., D28-1, up to 1.3%; Figure 2f [see also *Moorby et al.*, 1984]), but is also highly variable. Zn is generally expected to be fractionated in hydrothermal systems through concentration in proximal sulfide deposits; the high Zn concentration in sample D28-1 may indicate formation at a proximal location, paucity of sulfide formation at depth, dissolution of previously formed sulfides, or higher Zn concentrations in the fluids than could be removed by sulfide precipitation. High Zn concentrations may be an important pathfinder element for nearby massive sulfide deposits [see also *Boyd et al.*, 1993]. This may also be true for especially high concentrations of other typically sulfide-hosted elements such as Cu, Pb, Mo, and Cd, also of Co and Ni if a hydrogenetic component can be ruled out.

[44] Several samples have unusually high Co contents compared to other hydrothermal Mn deposits [*Hein et al.*, 1997], which is the element considered most characteristic of hydrogenetic precipitation [*Halbach et al.*, 1983]. However, the samples (D8-5A, D8-12A, D8-12C, D33-2-1, D33-2-2, and D33-2-3) with high Co (501–1169 ppm) are clearly hydrothermal and the high Co is probably hydrothermal and associated with high Fe contents. The three D33 samples are vein fill and cement that were isolated from strongly altered breccias. If the Co was adsorbed from seawater near the seabed after mineralization of the sediment, then the middle layer (D8-12B) of the three layers (D8-12A, D8-12B, D8-12C) of sample D8-12 should have high Co contents like the adjacent layers, but it does not, even if the data are normalized for the higher aluminosilicate fraction in sample D8-12B (Table 2). A more likely explanation is that the hydrothermal component of each layer represents a different hydrothermal pulse, each with a different composition. We suggest that samples with high Co contents might reflect mineralization from relatively higher temperature hydrothermal fluids.

[45] The abundance of Fe increases with decreasing Mn: Subgroup 2B (mean 0.89% Fe), Subgroup 2A (4.23% Fe), Group 1 (8.39% Fe). However, the relative proportion of hydrothermal Fe (excess Fe over detrital Fe based on Fe/Al ratios compared to arc volcanic rocks) changes very little among the three sample groups: From 55% of the total Fe for Subgroup 2B samples, to 58% for Subgroup 2A samples, to 49% of the total Fe for Group 1 samples; the proportion of hydrothermal Fe to total Fe is remark-

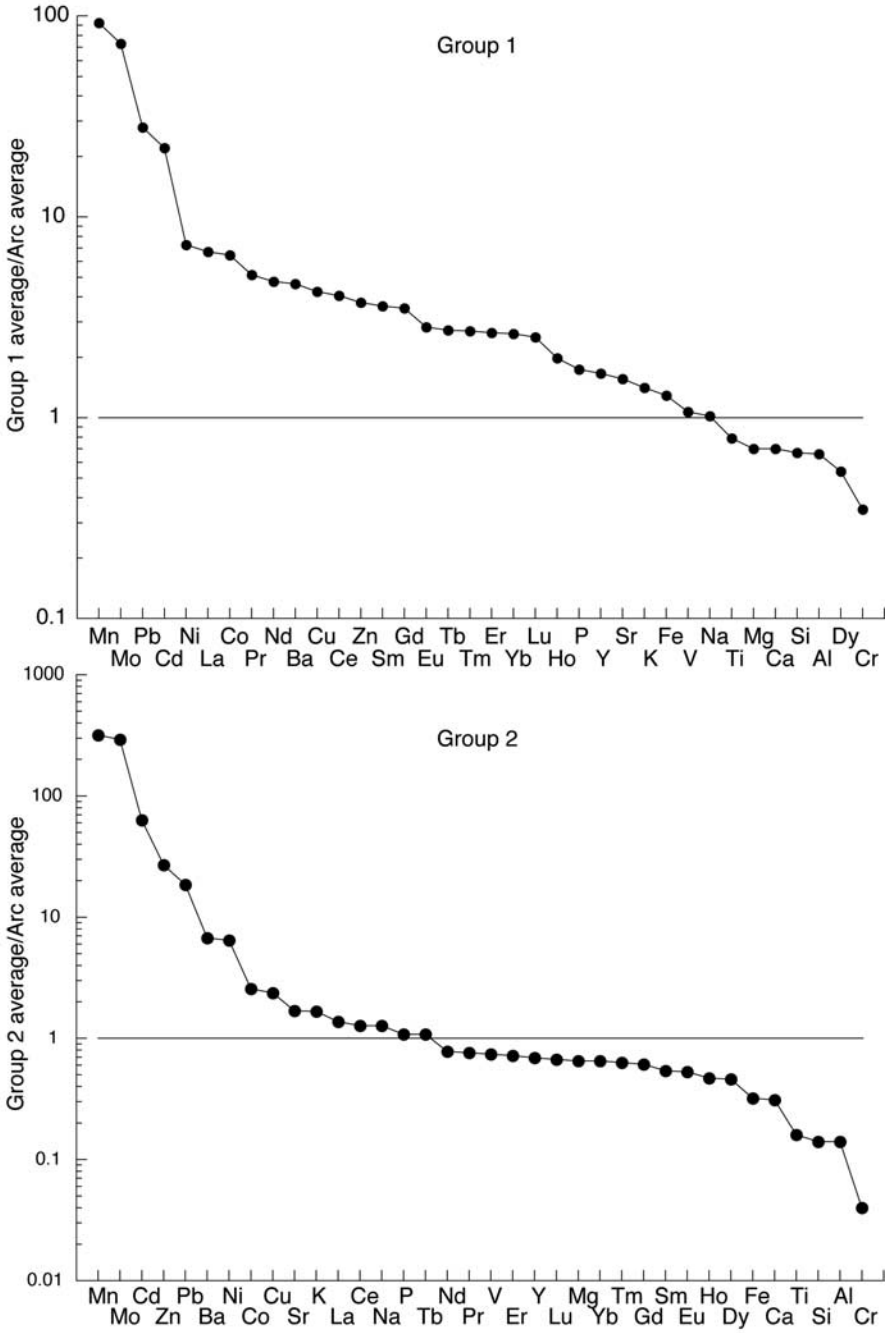

Figure 6. Element enrichment diagrams for Groups 1 and 2 sample data relative to average volcanic rock composition for the Mariana arc volcanoes from which our samples were taken (see Tables 2 and 6).

ably constant (49–58%), regardless of the degree of Mn mineralization.

[46] Groups 1 and 2 and Subgroups 2A and 2B mean compositions, normalized to the mean composition of volcanic rocks from the Mariana arc (Figure 6 and Table 6), show that Mn, Mo, Pb, and Cd are consistently 1–2 orders of magnitude enriched in the Mn deposits. Zn is also included with those elements for Group 2 samples as a whole and Subgroup 2B specifically. Mn consistently has the highest enrichment factor (up to about 400 times for Subgroup 2B), Mo is next, and then Cd is third highest except in Group 1 samples where Pb has the third highest enrichment. Other elements that are consistently enriched (up to 9 times) over Mariana arc volcanic rocks include Zn, Ni, Ba, Co, Cu, K, Sr, La, P, and Ce; and only in the low Mn samples (Group 1), all the REEs and Y. Ce is probably concentrated by oxidation on the surface of the Mn minerals in all sample groups, whereas the REEs in general are probably sorbed on the Fe oxyhydroxide in the low Mn, high Fe samples (Group 1).

Table 6. Mean Chemical Composition for Mariana Arc Volcanic Rocks From Seamounts for Which Samples Were Collected for This Study[a]

	Value
Fe	6.51
Mn	0.134
Si	25.2
Al	8.91
Mg	3.00
Ca	6.93
Na	2.04
K	0.657
Ti	0.480
P	0.063
B	19.8
Ba	210
Be	0.732
Cd	0.280
Co	35.0
Cr	97.7
Cs	0.395
Cu	98.5
Ga	16.3
Hf	1.73
In	0.051
Mo	2.02
Nb	1.53
Pb	3.13
Rb	14.9
Sc	34.8
Sr	322
Ta	0.105
Th	0.793
U	0.352
V	257
Y	22.5
Zn	76.3
Zr	35.0
La	6.47
Ce	14.3
Pr	2.03
Nd	9.68
Sm	2.75
Eu	0.931
Gd	3.18
Tb	0.790
Dy	3.51
Ho	1.05
Er	2.25
Tm	0.330
Yb	2.19
Lu	0.353

[a]Here n = 38 samples (R. J. Stern, unpublished data, 2007). Major elements are in percent (or weight percent), and minor elements are in ppm.

4.4.1. End-Member Components

[47] On the basis of the (Co + Ni + Cu)x10-Fe-Mn ternary diagram, most of the Mariana arc samples fall within the hydrothermal field (Figure 7a). Subgroup 2B samples occur at the Mn apex with Subgroup 2A and then Group 1 samples moving consecutively through the hydrothermal field toward the Fe apex. One sample from Group 1 falls within the hydrogenetic field because of unusually high Co and Ni contents. Two samples from Group 1 and most of the Fe-Mn crusts from the Mariana arc fall in the hydrogenetic/hydrothermal transition zone. It should not be construed that the samples that fall outside the hydrothermal field are not hydrothermal or not predominantly hydrothermal; rather, it is the result of the unusual hydrothermal compositions of a few samples as pointed out above.

[48] Most samples can be modeled using a three-component system with aluminosilicate, Mn oxide, and Fe oxyhydroxide end-members. Only the Mn oxide end-member is found in nearly pure form. This relationship is shown on a (Si)x2-Fe-Mn ternary plot, where most of our data fall near a line connecting the mean arc volcanic rock datum with the Mn apex (Figure 7b). Data that do not fall along that line have a relatively greater Fe component, the amount of which generally increases from Subgroup 1B through Group 1 samples. These relationships can also be seen on scatterplots of Si + Al versus Mn and Fe (Figures 7c and 7d). For Si + Al versus Mn, nearly all the data fall on or below a line connecting mean volcanic arc rocks and the highest Mn sample, with an increasing deviation from that line going from Subgroup 2B through Group 1 samples. This shows that most samples are depleted in Si + Al relative to a two-component aluminosilicate/Mn oxide mixing system. In a plot (not presented) of Mn versus Fe + Si + Al, a single regression line passes statistically through all Groups 1 and 2 data points and shows that Mn has a nearly perfect negative correlation ($r^2 = 0.97$, n = 60) with the aluminosilicate plus Fe oxyhydroxide components. A plot of Si + Al versus Fe clearly shows that nearly all samples are enriched in Fe relative to a mixing line connecting arc volcanic rocks and Mn oxide end-members (Figure 7d), which is also true in a plot of Fe + Si + Al versus Fe. Many of the samples from Groups 1 and 2 show a positive correlation between Fe and Si + Al; however, the Group 1 Mn sandstones taken separately show a negative correlation between Fe and Si + Al (Figure 7d). This emphasizes the fact that Fe is about equally distributed between the aluminosilicate and hydrothermal end-members.

4.4.2. Rare Earth Elements

[49] Total REE concentrations are generally very low, consistent with a hydrothermal origin. Subgroup 2B samples have the lowest total REE concentrations. Chondrite- and shale-normalized REE patterns (Figure 8a) show that some Group 1 samples have patterns similar to that of the mean volcanic arc rocks (i.e., sample D8-1) and others similar to that of the mean mixed hydrothermal-hydrogenetic Mariana arc Fe-Mn crust samples (i.e., D8-20). Those differences reflect the ratio of Mn cement to framework grains and growth rates. Subgroup 2A samples generally show less enrichment in REEs than the arc volcanic rocks, but have similar normalized patterns to arc rocks (Figure 8b). Sample D3-3 from Subgroup 2B has the lowest relative enrichment of REEs, with 9 of the 15 elements below their detection limits (Table 7 and Figure 8c). The other Subgroup 2B samples have normalized enrichments similar to those of the arc volcanic rocks; the normalized patterns are also similar, with the exception that all three Subgroup 2B samples have negative Ce anomalies, as do most of Group 1 and Subgroup 2A samples. Sample D55-3 is depleted in La, which produces an apparent positive Ce anomaly. A better measure of the Ce anomaly for that sample would be the shale-normalized Ce/Pr ratio, which indicates a negative Ce anomaly; this would not be true for sample D44-1, which appears to be the only sample with a positive Ce anomaly. A positive Eu anomaly occurs in most

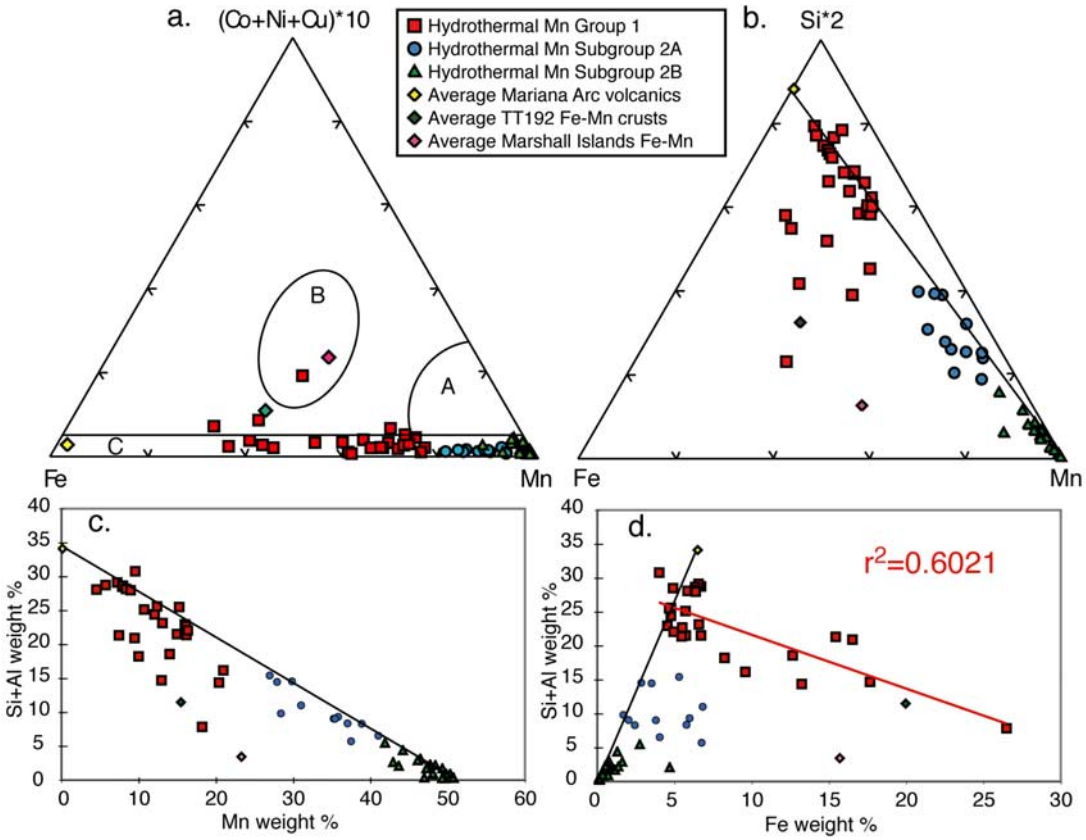

Figure 7. (a) Fe-Mn-(Co + Ni + Cu)x10 ternary diagram for 24 samples from Group 1, 11 from Subgroup 2A, and 21 from Subgroup 2B, and average compositions for Mariana arc volcanic rocks (Table 6), Fe-Mn crusts from cruise TT192 [*Hein et al.*, 1987], and Fe-Mn crusts from the Marshall Islands [*Hein*, 2004]; field A is diagenetic, field B hydrogenetic, field C hydrothermal (fields modified from *Bonatti et al.* [1972]); (b) Fe-Mn-(Si)x2 ternary diagram for sample data as in Figure 7a; a line is drawn through the highest Mn sample and the average arc volcanic rock; (c) Mn versus Si + Al concentrations for 60 samples from Groups 1 and 2; a line is drawn through the highest Mn sample and the average arc volcanic rock; (d) Fe versus Si + Al concentrations for 60 samples from Groups 1 and 2; the red line is a regression through Group 1 samples, and the r^2 value shows a statistically significant negative correlation at a greater than 99% confidence level. The black line is drawn through the highest Mn sample and the average arc volcanic rock.

shale-normalized patterns and a small negative anomaly on chrondrite-normalized patterns, both reflecting the patterns of mean arc rock. These data suggest that end-member hydrothermal fluids were of moderate temperatures, probably less than about 250°C [e.g., *Glasby et al.*, 1997]. The patterns for the hydrothermal samples are generally light REE enriched on chondrite-normalized patterns and heavy REE enriched on shale-normalized patterns. Overall, the REEs are derived predominantly from leaching of arc rocks by hydrothermal fluids (and incorporation of volcaniclastic material) and rarely from seawater. This can be seen from the Y/Ho ratios, where all samples but one fall within the range of volcanic rocks/shales (20–35, mean 28), rather than near that of seawater (45–75, mean 57) [*Bau et al.*, 1996]. The negative Ce anomalies indicate rapid precipitation of the Mn oxides, which is consistent with growth rate calculations (see below); the general increase in its magnitude with increasing Mn content reflects increasing rates of growth.

4.4.3. Platinum Group Elements

[50] Pt, Pd, and Rh concentrations vary from below their limits of detection to maximum values of 88 ppb (mean 16.5), 16 ppb (mean 3.7), and 41 ppb (mean 3.6), respectively. Pt and especially Rh are enriched and Pd is about the same compared with concentrations for Mariana arc volcanic rocks of 8.5 ppb Pt (2–55 ppb, n = 17; mean 5.6 ppb if 55 ppb outlier not used), 4.1 ppb Pd (<1–13 ppb; 3.6 ppb if 13 ppm outlier not used) and <1 ppb Rh for all samples (J. R. Hein, unpublished data, 2006). In contrast, mean Pt values for hydrogenetic Fe-Mn crusts from the central Pacific vary from about 150 to 800 ppb and Rh values from about 10 to 15 ppb [e.g., *Hein*, 2004]. The Mariana stratabound deposits and hydrogenetic Fe-Mn crusts have about the same mean concentrations of Pd. Pt correlates with Fe and elements associated with Fe, which is probably the dominant host for Pt, whereas Pd correlates only with Ba and is likely partitioned among several phases. The concentration of Os was determined by *Burton et al.* [1999]

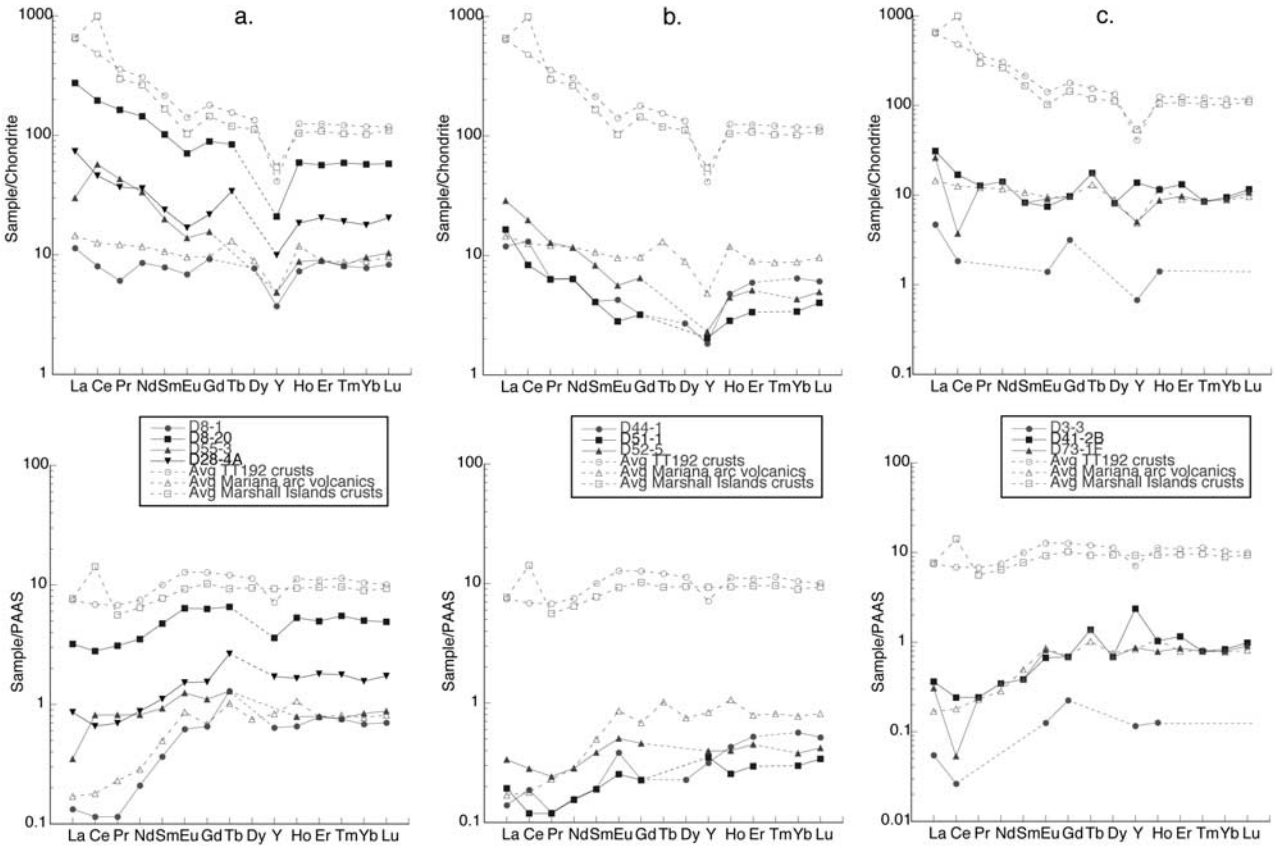

Figure 8. Rare earth element plots for (a) Group 1, (b) Subgroup 2A, and (c) Subgroup 2B, normalized to (top) chondrites [*Anders and Grevesse*, 1989] and (bottom) shale-PAAS [*McLennan*, 1989]. For elements below the detection limit, the sample symbol is left out and connecting lines dashed.

for one of the stratabound Mn samples (D20-1) and was very low, 0.07 ppb, more than an order of magnitude lower than Os concentrations in hydrogenetic Fe-Mn crusts, 1.0 to 3.6 ppb [*Burton et al.*, 1999]. These data suggest that platinum group elements (PGEs) are derived predominantly from leaching of basement rocks and that samples with relatively high PGEs may have a component derived from leaching of ultramafic rocks.

4.4.4. Statistical Correlations From Bulk Chemical Data

[51] Correlation coefficients for Subgroup 2B samples (n = 21) show no positive correlations between Mn and any other element, but Mn shows negative correlations with the aluminosilicate-associated elements (Si, Al, Ti, etc.) and Fe. Fe correlates with aluminosilicate elements (Si, Al, Cr), as well as Co; Fe has negative correlations with Mn and Na. Elements that correlate with Si and Al include Ti and Fe. These data indicate that the low concentrations of Fe in Subgroup 2B samples are partitioned between two phases, aluminosilicates and Fe oxyhydroxide, in agreement with calculations presented above. Cd, Zn, Cu, Pb, and Ni correlate with each other, but do not have a dominant (statistically significant) association with Fe, Mn, or Si-Al. They are probably partitioned among all those phases, but predominantly with the Fe and Mn minerals, and secondarily with aluminosilicates for Ni and Pb. In contrast, Co correlates with Fe and is probably associated predominantly with Fe oxyhydroxide. Mo correlates only with As, but is probably associated with the Mn minerals, as determined by others [*Glasby et al.*, 1997; *Rogers et al.*, 2001; *Koschinsky and Hein*, 2003; *Kuhn et al.*, 2003].

[52] As Mn concentrations decrease, the number of elements that correlate with Mn increases, such as from Subgroup 2B to Subgroup 2A samples then to Group 1 samples. Mn shows positive correlations with Co, Mo, H_2O^+, H_2O^-, and Na in Subgroup 2A samples and with LOI, H_2O^+, H_2O^-, Mo, K, Cd, and Ba in Group 1 samples. Co correlates with Mn in Subgroup 2A samples, but with Fe in Group 1 samples. Fe correlates with P, As, and Ba in Subgroup 2A samples and with P, As, Pb, Pt, LOI, H_2O^+, H_2O^-, Co, and Mo in Group 1 samples. These Fe correlations reflect elements associated with the Fe oxyhydroxide, rather than aluminosilicate minerals; in fact, Fe shows negative correlations with aluminosilicate-associated elements (Si, Al, Ca, Na) in Group 1 samples. Of the minor metals (Cd, Zn, Cu, Pb, and Ni), Cd correlates with Mn, and Pb with Fe in Group 1 samples; Zn, Cu, and Ni in Group 1 samples and all of them in Subgroup 2A samples do not show correlations with Mn, Fe, or Al-Si, and are probably partitioned among several minerals.

[53] Several elements show positive correlations with water depth, with Pb having the highest statistical significance; others include Fe/Mn, Na, Ti, Cr, Cu, V, Y, Ce, and Tb. The other REEs would correlate with water depth at

Table 7. Yttrium and Rare Earth Elements for 10 Hydrothermal Mn Samples and Mariana Arc Averages for Fe-Mn Crusts and Volcanic Rocks[a]

	Group 1				Group 2A			Group 2B			Average Fe-Mn Crusts	Average Volcanics
	D8-1	D8-20	D28-4A	D55-3	D44-1	D51-1	D52-5	D3-3	D41-2B	D73-1F		
La	5.08	122	32.9	13.4	5.33	7.38	12.8	2.10	13.9	11.7	284	6.47
Ce	9.14	223	52.4	64.8	14.9	9.48	22.5	2.10	19.2	4.26	547	14.3
Pr	1.02	27.3	6.16	7.20	1.07	1.05	2.14	<1	2.13	2.13	59.9	2.03
Nd	7.11	119	29.8	27.8	5.33	5.27	9.63	<2	11.7	11.7	254	9.68
Sm	2.03	26.3	6.16	5.14	1.07	1.05	2.14	<0.5	2.13	2.13	55.6	2.75
Eu	0.670	6.88	1.64	1.35	0.416	0.274	0.545	0.136	0.725	0.883	13.8	0.931
Gd	3.05	29.4	7.19	5.14	1.07	1.05	2.14	1.05	3.20	3.19	59.3	3.18
Tb	<1	5.06	2.05	<1	<1	<1	<1	<1	1.07	1.06	9.36	0.790
Dy	3.05	–	–	<1	1.07	<1	<1	<1	3.20	3.19	53.0	3.51
Y	17.3	97.2	46.2	22.6	8.53	9.48	10.7	3.14	64.0	23.4	193	22.5
Ho	0.650	5.26	1.64	0.782	0.426	0.253	0.396	0.126	1.02	0.777	11.2	1.05
Er	2.23	14.2	5.13	2.26	1.49	0.843	1.28	<0.5	3.30	2.45	31.2	2.25
Tm	0.305	2.23	0.719	0.309	<0.2	<0.2	<0.2	<0.2	0.320	0.319	4.61	0.330
Yb	1.93	14.2	4.41	2.37	1.60	0.843	1.07	<0.5	2.35	2.23	29.4	2.19
Lu	0.305	2.13	0.749	0.381	0.224	0.148	0.182	<0.05	0.426	0.394	4.36	0.353
∑REE	<54.81	694.64	197.05	<155.54	<43.74	<39.33	<67.71	<15.40	128.61	69.82	1609	72
Y/Ho	27	18	28	29	20	38	27	25	63	30	17	21
Ce*	0.921	0.894	0.834	1.560	1.433	0.731	0.951	0.345	0.770	0.192	0.966	0.943
La_N/Sm_N	1.447	2.694	3.088	1.505	2.895	4.052	3.474	2.427	3.763	3.184	2.958	1.361
Yb_N/Sm_N	0.989	0.561	0.746	0.479	1.562	0.833	0.521	1.042	1.146	1.094	0.551	0.827

[a]Rare earth elements values are in ppm. Normalized to 0% hygroscopic water. Ce* is calculated using chondrite-normalized data and the equation 2Ce/(La+Pr). LREE and HREE enrichments calculated using chondrite-normalized data.

somewhat below a 95% confidence level. K is the only element with a negative correlation with water depth. It is difficult to assess if those same elements change predictably with geographic location because water depth generally increases from west to east and from north to south and would have a greater influence than geographic location. However, Ni has no correlation with water depth but is generally higher in crusts from the easternmost part of the arc. This is interesting because that region is closer to the fore arc where serpentines are common, which typically have high Ni contents. High Ni in Mn deposits, along with high Cr, may reflect an ultramafic source (see section 5).

4.4.5. Grouping of Elements From Factor Analyses

[54] For Subgroup 2B (high Mn) elements, four factors account for 92% of the variance in the data set. Elements are listed in order of decreasing rotated factor scores. We interpret those factors to represent the aluminosilicate detrital fraction (Ti, Al, Si, Ni, Ce, Fe, Cr, Ba, Y, Co); and three Mn-bearing hydrothermal components that probably represent hydrothermal leaching of different materials: Sulfides (Pb, Zn, P, Cd, Cu, Mn, Mg, Na, and Ni), volcanogenic rocks and sediments (Na, Ca, As, Mo, Mn, Ce, and Si), and biogenic material (Mg, K, Mn, Ba, Sr, V, and Ca).

[55] For Subgroup 2A (high-Mn sandstones) elements, four factors account for 96% of the variance in the data set. We interpret those factors to represent the aluminosilicate detrital fraction (Al, Cd, V, Zn, Cr, Ti, Mg, Si, and Y); hydrothermal Fe oxyhydroxide (P, Ni, As, Ce, Co, Zn, K, Fe, Sr, and Pb); hydrothermal Mn (Mo, Cu, Na, Mn, Fe, Co, Si, Ba); and carbonate fraction (CO_2, Ca, Sr, Y, Mg, and Na). A carbonate factor is consistent with this subgroup showing the highest biocarbonate component.

[56] For Group 1 (low-Mn sandstones) elements, three factors account for 91% of the variance in the data set. We interpret those factors to represent the aluminosilicate detrital and carbonate fractions (Al, Cr, Ca, Si, Na, Ti, V, Mg, CO_2, and Y); hydrothermal Fe oxyhydroxide (P, Co, Fe, As, Ba, Ni, Mo, Sr, Zn, Ce, Mn, and Y); and hydrothermal Mn fraction (Cd, Mn, Na, K, Zn, Mg, Ba, Si, Al).

[57] Elements interpreted to be in a detrital factor consistently include Si, Al, Ti, Cr, and Y, and Mg and V in two of the three data sets; the Fe oxyhydroxide/Fe-bearing lithic phases consistently include Fe, Co, Ce, K, and Ni in all three data sets and P, As, Zn, and Sr in two of the three data sets; and the hydrothermal Mn consistently includes Mn, Ba, Na, and Si in all data sets and Mo, Cd, Cu, Zn, Mg, and K in two of the three data sets.

4.5. Growth Rates

[58] Growth rates of Mn mineralization were determined using the empirical equation of *Manheim and Lane-Bostwick* [1988]: Growth rate $R = 0.68/(Co^n)^{1.67}$, where normalized Co is $Co^n = Co \times 50/(Fe + Mn)$, and Co, Fe, and Mn are measured concentrations in weight percent. On average, the 21 Subgroup 2B samples have the highest growth rates, with five samples yielding rates of over 125,000 mm/Ma and three others over 14,000 mm/Ma (Table 8). Only one Subgroup 2B sample has a growth rate of <100 mm/Ma, 96 mm/Ma, which is the result of an anomalously high Co content in that sample. Growth rates for the remainder of samples in Subgroup 2B range from 465 to 8950 mm/Ma. Subgroup 2A samples range from 207 to 23,910 mm/Ma and Group 1 samples from 15 to 64,650 mm/Ma; if one outlier sample is not considered, the range would be 15 to 4700 mm/Ma. The low growth rates could indicate either a hydrogenetic component, or, as we favor for our samples, a hydrothermal Co source (see above), in which case the low growth rates would be spurious. Overall, the growth rates are typical of hydrothermal accretion of Mn oxides.

[59] The number of years required to accrete a Mn oxide layer can be determined from the growth rate and thickness of the layer mineralized. It should be emphasized that complete Mn sandstone beds were not always recovered and mineralization may have covered a thicker stratigraphic

Table 8. Growth Rates and Ages for 24 Samples From Group 1 and 32 Samples From Group 2

	Growth Rate (mm/Ma)	Age (ka)
	Group 1	
D8-1	852	47.0
D8-5A	15	4,127
D8-12A	18	570.4
D8-12B	1,804	6.65
D8-12C	23	345.8
D8-20	135	111.5
D13-1A	2,165	2.31
D15-1A	175	45.7
D28-3A	601	20.0
D28-4A	2,173	32.2
D28-6A	1,093	18.3
D31-1	2,353	2.13
D33-2-1	37	218.1
D33-2-2	20	–
D33-2-3A	>64,646	<0.31
D40-3A	1,025	29.3
D40-3B	839	17.9
D40-3C	576	29.5
D54-2	2,225	6.74
D55-3	4,695	6.39
D56-1B	798	37.6
D57-2	161	93.4
D57-4	60	416.1
D73-1A	2,109	42.7
	Subgroup 2A	
D12-2	23,912	0.04
D44-1	424	47.1
D44-1A	1,508	6.63
D44-3	300	113.3
D51-1	3,277	12.8
D52-4A	1,090	18.4
D52-4C	3,762	5.32
D52-5	269	223.0
D52-9A	912	43.9
D52-11	207	48.4
D56-2	2,768	14.5
	Subgroup 2B	
D3-1	8,005	0.87
D3-3	14,184	1.55
D3-5	7,271	3.44
D8-8	7,243	0.55
D11-1A	1,689	8.88
D20-1A	74,321	0.20
D28-1B	804	6.22
D28-1-CI	2,763	2.53
D28-1-CII	32,827	0.09
D28-1D	>219,125	<0.02
D28-1E	>227,820	<0.03
D28-1F	>218,213	<0.05
D28-1G	1,169	34.2
D33-2-3	96	20.9
D41-2B	8,949	4.47
D52-4B	465	32.2
D52-9B	1,391	2.88
D52-10	2,263	4.42
D55-4	5,616	5.34
D56-4	>227,335	<0.11
D73-1F	125,437	0.24

interval for some samples. Durations of mineralization range from 23 years for a 5-mm-thick stratabound Mn layer to 4 Ma for a 60-mm-thick Co-rich, Mn sandstone layer, which is a distant outlier value. The next longest duration is about 0.5 Ma, for a 10-mm-thick Mn sandstone layer, which would not be greatly different from the above duration for a layer of equivalent thickness. However, the longest durations are the result of calculations from high Co samples, which may not give reliable results. The fastest growth rate, which is a minimum rate for D28-1E, yields 30 years (a maximum estimate) to accrete a 6-mm-thick stratabound Mn layer; sample D56-4 has the next fastest rate, which took about 110 years to accrete a 25-mm-thick layer.

4.6. Petrography of Host Sedimentary Rocks

[60] Most sandstones and breccias are composed of volcaniclastic debris derived from the arc volcanoes; the remainder are foraminifera-bearing sandstones and foraminiferal limestones that contain minor volcaniclastic debris. Unaltered samples are composed of detrital plagioclase, clinopyroxene, and minor olivine, orthopyroxene, amphibole, and quartz. Mineral grains are commonly euhedral. Pyroxene and plagioclase are commonly twinned and zoned, and less commonly embayed. Volcanic rock fragments and fresh volcanic glass fragments are present in all thin sections analyzed. On the basis of planktonic foraminifera and nannofossil species, most of the fossil-bearing sandstones are of Quaternary age (D8-2; D11-1; D55-6; D56-1; D56-2; D58-1; D73-1), although some could only be assigned a range of late Pliocene or Quaternary (D36-5; D42-3) (J. R. Hein, unpublished data, 1986). Mn mineralization in all dated samples is therefore relatively recent, less than 1.8 Ma.

[61] A total of 100 framework grains were counted for each of nine polished sections to classify the sandstones. Point counts were not done on stratabound Mn layers, breccias, or silty mudstones. With one exception, data plot within the undissected arc field of the quartz-feldspar-lithics diagram of *Dickinson et al.* [1983] (Figure 9). The exception is a sandy siltstone (D28-6) that plots in the transitional arc field. This sample is from the west side of the cross-chain seamount, located west of Uracas Seamount. Its anomalous composition is due to its fine grain size, which discriminates against the incorporation of and identification of lithic fragments. However, the presumably greater age of cross-chain seamounts at their western end may also be reflected by the sediment composition. Several sandstones with unusual grain types were identified. One of these, a coarse-grained sandstone (D28-2), contains the typically altered volcanic rock fragments, plagioclase, and pyroxene grains, but also contains clasts of iron-rich mud, detrital barite, and detrital grains of polycrystalline quartz (presumably of hydrothermal origin). The provenance of this sandstone appears to have been in part a hydrothermal deposit.

[62] The delicate structure of detrital glass in several thin sections indicates little or no transport before deposition. Dredge haul D73 recovered sandstones with vesiculated and fragile volcanic glass fragments as a major component. These sandstones have minor lithic fragments with both broken and euhedral mineral crystals. Sample D73-1D is a graded sandstone with coarse lithic fragments grading into fine-grained glass and mineral fragments. Petrographic and hand sample textures of D73 sandstones are indicative of an eruptive center facies; and microprobe analyses of volcanic glass from samples D73-1D and D73-1A indicate derivation from two or more eruptive events. The glass fragments of this dredge follow a compositional trend that shows deri-

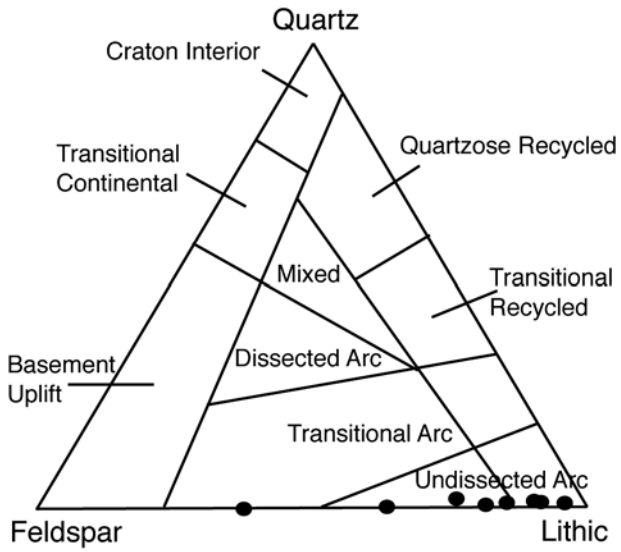

Figure 9. Point counted sandstone samples plotted on a ternary diagram with provenance fields of *Dickinson et al.* [1983].

vation from the same parent magma [*Schulz and Hein*, 1991]. These samples probably represent reworked detritus from several eruptive phases of a single eruptive center.

[63] Minor alteration of clastic grains occurs in every sample and involves the breakdown of volcanic glass and volcanic rock fragments to clay minerals (generally smectite) and palagonite. However, alteration cannot be attributed exclusively to Mn-bearing hydrothermal fluids, and both halmyrolysis and the mineralizing fluids played roles.

[64] The alteration of glass and volcanic rock fragments in samples D28-2 and D73-1D can be directly attributed to the mineralizing fluids. Sample D28-2 has a dense laminated stratabound layer of Mn oxide at the base that is overlain by volcanic rock fragments. The most highly altered volcanic rock fragments occur immediately above the stratabound layer. Sample D73-1D has a crosscutting fracture filled with dense Mn oxides. The volcanic glass fragments to either side of the fracture are highly altered to a greenish-yellow clay mineral (smectite?), whereas away from the fracture the glass is less altered. In both samples, the greatest alteration occurred near the fluid pathways.

[65] Grains in Mn sandstones were first coated by Mn oxides, thereby forming a fine-grained, massive rim cement, and the remaining void space was then filled by coarser-grained Mn oxides (Figure 10a). Replacement of mineral grains by Mn oxides (Figure 10b) was rare compared to replacement of foraminifera (Figure 10c) followed by radiolarians. Molds of foraminifers and radiolarians are very common. Molds formed when mineralizing fluids precipitated Mn oxides around and in fossil tests, which preserved their fine structure and ornamentation, and produced internal and external casts after the tests dissolved (Figure 10d).

5. Discussion

[66] Hydrothermal Mn deposits have been found along all active volcanic arcs in the west Pacific such as the Kuril arc [*Gavrilenko*, 1997; *Glasby et al.*, 2006], Izu-Bonin arc [*Usui et al.*, 1986, 1989], Yap-Belau arc [*Hein*, 1992; *Hein et al.*, 1999], Tonga/Kermadec arc [*Cronan et al.*, 1982; *Moorby et al.*, 1984; *Hein et al.*, 1990], and the Mariana arc, as described here. Hydrothermal, diffuse flow Mn mineralization is perhaps the most widespread type of mineralization in active arcs, at least in the near-surface environment. Mn mineralization is found in volcanic arcs elsewhere in the world as well, for example the Lesser Antilles active arc and Aves Ridge (remnant arc) of the eastern Caribbean [*Kang and Kosakevitch*, 1984]. All of these submarine arc-hosted Mn oxide deposits have similar chemical compositions, such as strong fractionation of Fe and Mn and generally low, but occasionally high, trace element contents, especially Li, Mo, Cd, Zn, and Pb. Texturally, the Mn mineralization is nearly identical throughout the global active arc system [e.g., *Cronan et al.*, 1982; *Usui and Nishimura*, 1992a, 1992b] and also in other tectonic settings with hydrothermal systems such as active hot spot volcanoes [e.g., *Hein et al.*, 1996], back-arc basins [e.g., *Kuhn et al.*, 2003; *Moorby et al.*, 1984], and mounds located both on-axis [*Scott et al.*, 1974; *Thompson et al.*, 1985] and off-axis of spreading ridges [e.g., *Moore and Vogt*, 1976; *Fitzgerald and Gillis*, 2006]. The global distribution of samples of similar occurrence and compositions indicates that the processes of formation of stratabound Mn deposits are broadly applicable to all modern arc systems.

[67] These stratabound hydrothermal Mn deposits have been mistakenly called crusts in many studies. They do not encrust anything, and do not generally form as a crust on the seabed, but rather are Mn oxide-impregnated sediment; that is they are predominantly sediment-hosted (more rarely basalt-hosted) stratabound and also predominantly stratiform deposits. Textural evidence shows that the Mn was supplied in up-flow systems and precipitation occurred within the sediment, albeit within the uppermost layer of sediment in some places. Once the hydrothermal fluids enter the water column, they rapidly adsorb metals from seawater and become in part hydrogenetic, a characteristic that increases with distance from the hydrothermal source [e.g., *Manheim and Lane-Bostwick*, 1988]. Once the fluids enter the water column, the Fe-Mn deposits that form from those fluids no longer have the same textural (or chemical) characteristics as the sediment-hosted stratabound deposits, even if they precipitated very near the discharge zone; these mixed-origin deposits are properly called crusts and have both hydrothermal and hydrogenetic components. The metallic/submetallic luster that characterizes stratabound Mn is not found in the mixed-origin crusts.

[68] The stratabound hydrothermal Mn deposits are exposed at the seabed in some areas, which is the result of either cementation of the uppermost sediment layer, or more commonly as the result of exposure through erosion and mass wasting of the uppermost unmineralized sediment that overlies the stratigraphically highest Mn-cemented bed. Mass wasting around submarine arc volcanoes is very common [e.g., *Cronan et al.*, 2002; *Draut and Clift*, 2006]. Many of the deposits are also associated with faults, which uplift deposits formed at some depth. These processes can result in a Mn oxide hard ground-like seabed and hydrogenetic and mixed hydrogenetic-hydrothermal crusts commonly grow on the stratabound Mn deposits if they do become exposed. Sr and Li in stratabound hydrothermal Mn

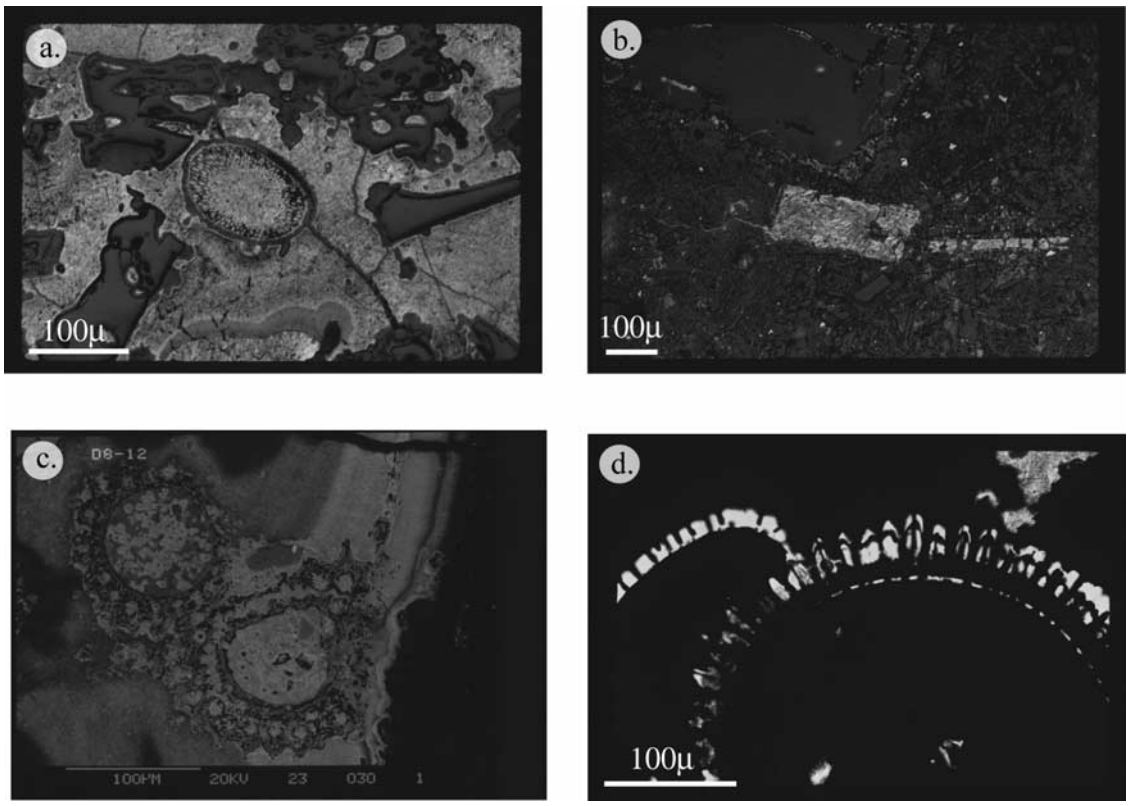

Figure 10. Thin section and SEM photomicrographs: (a) Mn oxide cemented sandstone, reflected light; the radiolarian at the center is completely coated by microcrystalline to crystalline Mn oxides, with colloform AC Mn oxides at the bottom center; the other clasts are unaltered glass fragments with Mn coatings, D73-1D; (b) reflected light, a pyroxene grain in an altered volcanic rock is replaced by Mn oxides, D33-2-3; (c) SEM backscatter electron image of a partly replaced foraminifera from stratabound layer D8-12; the Mn oxides penetrated the foraminiferal test; calcite is still present in several areas but is degraded; (d) foraminifera mold, the original calcite test dissolved leaving the fine structures preserved in Mn oxide, D8-27.

exposed at the seabed can exchange isotopically with seawater Sr and Li [*Chan and Hein*, 2007], whereas other elements' (i.e., Pb, Hf, Tl, Os) isotopes apparently do not exchange with seawater.

5.1. Sediment Bodies and Pathways of Mineralization

[69] Mn-mineralized sediment was recovered from the outer flanks, summit areas, and inside the caldera of submarine volcanoes along the IBM arc. All IBM stratabound deposits are hosted by sandstone and volcanic and sedimentary breccias, which were the most common non-lava rock types collected during cruise TT192; other mineralized rock types include pyroclastic and biogenic deposits. Sediments that compose the dominant rock types were deposited by slumping, debris flows, turbidites, and other mass wasting processes, and were redistributed by bottom currents in some places. The volcanic glass and delicate grains found in the sandstone samples indicate that the sediment was not transported very far. *Draut and Clift* [2006] found a pattern of mass wasting that occurs for about 20 km around each caldera that they studied along the southern Mariana arc. The distribution of sediment and the sediment types deposited on arc volcanoes must also have changed as the volcanoes grew and degraded through their life cycle and as the result of caldera collapse.

[70] The thickness of the sediment that overlies volcanic basement and the thickness of the sedimentary sections that were mineralized are for the most part unknown. That information is needed to determine the size of the reservoir in which Mn oxides can accumulate and the amount of mineralization that occurred. A potential analog example in the geologic record (Milos Island, Greece) has a sediment thickness of 35 to 50 m and about 35 to 40% of the beds in that section were mineralized (see section 5.4). Hyaloclastite and volcaniclastic sediment on the Mariana volcanoes can be up to several meters thick even around the summit of volcanoes, on caldera walls, and on caldera cinder cones and lava domes.

[71] The stratabound Mn was deposited within the sedimentary sections as determined by data collected here, but also likely occurs deeper in the sections as stockwork veins in the volcanic basement and sediment. Mn preferentially precipitated adjacent to fractures and faults, along bedding planes, and in coarse-grained sediments, especially if capped by a finer-grained lithology. Trace metals in the Mn deposits were derived predominantly from leaching of

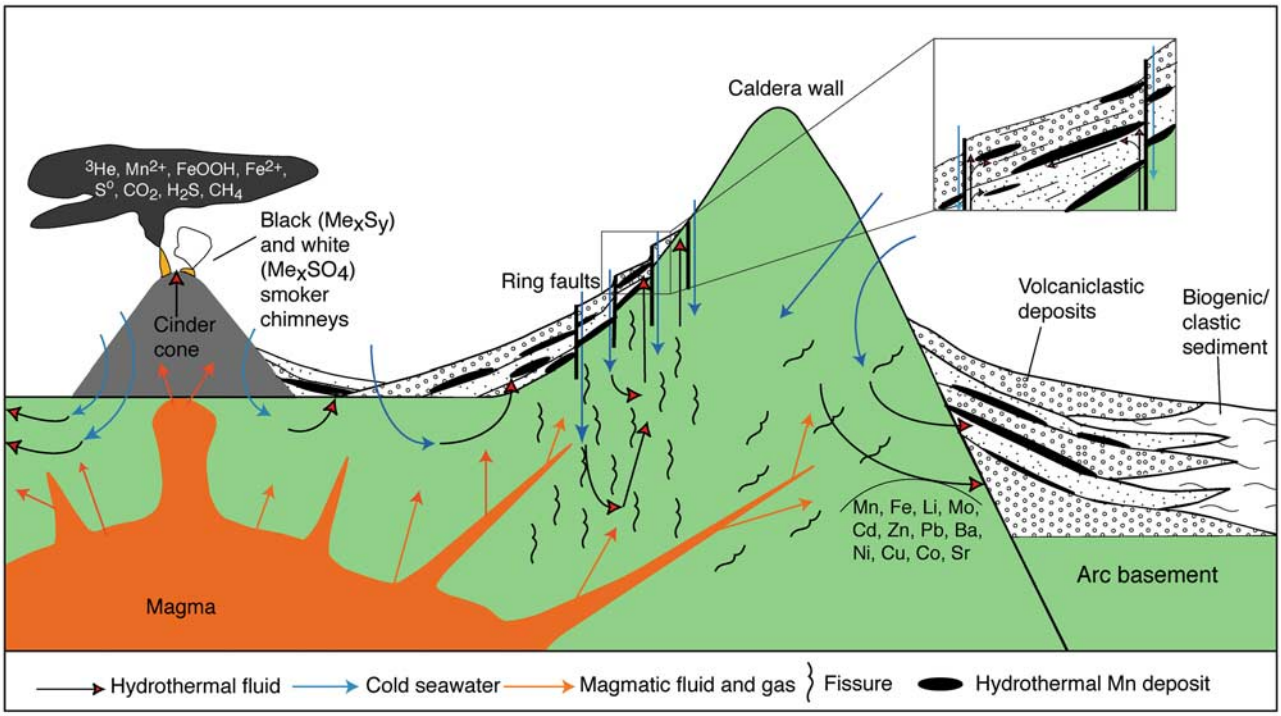

Figure 11. Schematic genetic model for the formation of hydrothermal Mn around a submarine caldera in an active volcanic arc setting. Mn is predominantly deposited within the volcaniclastic/pyroclastic/biogenic sedimentary sections as determined by data collected here, but also probably occurs as stockwork veins in the near-surface volcanic basement and sediment sections. Mn precipitates preferentially adjacent to fractures and faults, along bedding planes, and in coarse-grained sediments. Fe oxyhydroxides precipitate in more proximal locations both within the sediment section and in the volcanic basement; however, depending on the conditions, Mn and Fe can vent directly into the water column and not be precipitated as stratabound deposits. The dominant sediment types are coarse-grained sandstones and both primary volcanic and sedimentary breccias, which were deposited by slumping, turbidity flows, and other mass wasting processes, and were redistributed by bottom currents in some areas. The thickness and extent of the sedimentary deposits are not known but, based on analogs in the geologic record, may be up to a few tens of meters thick and unevenly distributed on the seamounts depending on currents, biological productivity, and tectonic/volcanic activity. Hyaloclastite and volcaniclastic sediment can be up to several meters thick even along the summit of caldera walls, cinder cones, and lava domes. Trace metals in the Mn deposits were derived predominantly from leaching of basement rocks of various compositions (ultramafic through rhyolitic), leaching of the volcaniclastic/biogenic sediments, and magmatic fluids and gases. Mineralizing hydrothermal fluids made up of mixed magmatic and seawater components were driven by heat from magma bodies, dikes, and sills. We speculate that dikes and sills probably penetrated the sediment in places and generated sediment-hosted hydrothermal circulation cells.

basement rocks of various compositions (ultramafic through rhyolitic), leaching of the volcaniclastic and biogenic sediments, and mixing of the seawater-dominated hydrothermal fluids with magmatic fluids and gases (Figure 11).

[72] Fe oxyhydroxides are known to precipitate in more proximal locations than Mn oxides, which would be located both within the sediment section and volcanic basement in the systems studied here; however, depending on the volcanic/hydrothermal conditions, both Mn and Fe can vent directly into the water column and not precipitate as stratabound deposits [see also *Malahoff et al.*, 2006]; diffuse flow Fe oxyhydroxides can also precipitate on the seabed associated with bacterial mats (2004 ROV observations by J. R. Hein et al. (unpublished data, 2004)). Close associations (interlaminations, mounds) of Fe oxyhydroxides and Mn oxides in some samples reflect fluctuating redox and temperature conditions of the mineralizing fluids.

[73] The relatively minor textural and mineralogical changes of the host rocks induced by the mineralizing fluids argue against the possibility of high fluid temperatures during mineralization. In most samples, fresh volcanic glass is cemented by Mn oxides. Volcanic glass degrades readily to palagonite or clay minerals under ambient temperatures and pressures on the seafloor, and degradation is enhanced with increased temperatures. If mineralizing fluid temperatures were high (>150°C), unaltered volcanic glass would be rare. The alteration minerals, Mn minerals, and textures indicate that Mn mineralizing fluid temperatures were relatively low, less than 125°C.

5.2. Model of Mineralization

[74] Mn oxide mineralization within arc volcanoes can be produced through various types of circulation cells. For example, generally shallow, low-temperature hydrothermal convection cells within the sedimentary prisms on the flanks and within calderas of active volcanoes can produce diffuse flow Mn oxide precipitates at shallow subsurface depths; these small-scale systems (tens of meters) can be driven by the heat from dikes and sills, or from more distant magma bodies [see also *Kinoshita et al.*, 2006]. Larger hydrothermal systems (100s of meters to kilometers) developed within the volcanic edifices from the heat of magma bodies can also generate fluids from which diffuse flow, low-temperature Mn oxides precipitate at shallow subseafloor depths and high-temperature sulfides/sulfates precipitate at depth. These larger systems can also form sulfides/sulfates at the seabed in the form of black and white smokers, in which the hydrothermal Mn and Fe are vented into the water column (Figure 11).

[75] The large chemical variations of trace elements such as Li, Mo, Ni, Cu, and Zn in the Mn oxide deposits, both within single beds and among deposits from different volcanoes, reflect depth (or size) of the hydrothermal system, which is related to the longevity and depth of the heat source, as well as rock/water ratio, source rock composition, permeability of the volcanic edifice, contributions of magmatic fluids and gas, precipitation of sulfides, sulfates, and Fe oxyhydroxides at depth, temperature, pH, and salinity of the hydrothermal fluid, and phase separation, which can occur at relatively low temperatures (<250°C) at shallow water depths. Fall-out from black smoker hydrothermal plumes can also form Mn oxide deposits, but not the stratabound types described here in which the mineralizing fluids were clearly part of up-flow systems.

[76] Sample textures indicate that the initial stage of mineralization was cementation of sediments by Mn oxides, which proceeded from forming rim cement on grains to completely filling pore space and finally replacement of grains in the most advanced stages. This cement has the highest amount of hydrothermal Fe, although the proportion of hydrothermal Fe to total Fe is nearly the same in all the stratabound deposits. As precipitation continued and porosity of the sediment decreased, the movement of mineralizing fluids became confined to fractures, faults, and other avenues of less resistance, such as along bedding planes. The concentration of mineralizing fluids along zones of less resistance led to the precipitation of high-grade stratabound layers within the Mn oxide cemented sediment, within otherwise unmineralized sediment, and within vugs and fractures.

[77] Generally, Mn oxide cement and stratabound Mn oxide layers and lenses are younger with depth in the sediment, that is, away from the seawater/sediment interface, based on textural data (orientation of columnar, botryoidal, scalloped structures); this conclusion is consistent with the limited radiometric dating available, which has been determined for only two deposits [*Cronan et al.*, 1982; *Usui et al.*, 1989]. The subbottom depth at which cementation began is not known, but is likely to have been within a few meters of the seabed, and in places was at or very near the seafloor/sediment interface, where the ascending fluids mixed with oxygenated interstitial waters. As the porosity decreased, thereby blocking the egress of diffuse flow fluids, precipitation occurred deeper in the sediment column creating younger Mn oxides beneath older ones. Those deeper layers may have been fed laterally from more focused flow along fractures. Some stratabound Mn layers were fractured and others were brecciated, which were then cemented by later stage Mn oxide. This sequence demonstrates repeated episodes of injection of hydrothermal fluids and fracturing and healing by filling fractures and vein formation as part of the mineralization. Fracturing was probably caused by both fluid pressure (hydrofracturing) and seismic activity. This simple model does not explain completely the variety of cementation textures found in IBM arc samples, but it is a reasonable first-order approximation.

[78] The characteristic bedding and lamination of the stratabound deposits indicate that individual beds formed from multiple episodes of precipitation. This occurred on large and small scales, through a sequence of beds, through single beds, and at the micrometer scale within laminae. On the submillimeter scale, variations in chemical and mineralogical compositions reflect the waxing and waning of single hydrothermal pulses, and on the millimeter scale, different pulses of hydrothermal fluids within a single hydrothermal phase; these pulses probably had different ratios of source components and probably differing temperatures, Eh, and pH as evidenced by the chemical variations in our samples. The waxing and waning of individual hydrothermal pulses explains the intercalation of AC oxides (rapid precipitation, waxing stage), and microcrystallites and crystallites (slower precipitation, waning stages) within the Mn oxides. This process also manifests itself in alternating massive (rapid precipitation, waxing stage) and porous-fibrous layers (slower precipitation, waning stage), which has been noted for other hydrothermal stratabound Mn deposits [e.g., *Hein et al.*, 1991]. These mineralogical/textural changes are accompanied by chemical changes that reflect the oxidation potential, temperature, and element concentrations in the mineralizing fluid, and growth rates and kinetics of the reactions.

[79] Different source components can be gleaned from the Q-mode factors, which suggest that there were contributions from the leaching of igneous rocks of different compositions, and minor inputs from biosiliceous and biocarbonate sediments including organic matter in places. The leaching of various proportions of the source rocks in different areas, combined with the precipitation of sulfides (or lack thereof) at depth and the leaching of sulfides at depth, can explain the variety of large- to fine-scale changes in chemical composition found in the hydrothermal Mn deposits. Elements that characterize the diffuse flow deposits studied here include Mn, Fe, Li, Mo, Cd, Zn, Pb, Ba, Ni, Cu, Co, Sr, K, and Na. Most of these elements can reflect multiple sources and therefore discriminant plots to identify various source components are not precise. However, high Ni plus Cr contents probably reflect the incorporation of a detrital ultramafic component or the leaching of ultramafic rocks, which for the IBM and Yap arcs would include serpentinites. Stratabound Mn deposits from the Yap arc are especially enriched in those two elements (Figure 12) and serpentinite was recovered in the same dredge haul as the hydrothermal Mn [*Hein et al.*, 1992]. Unfortunately, Ni

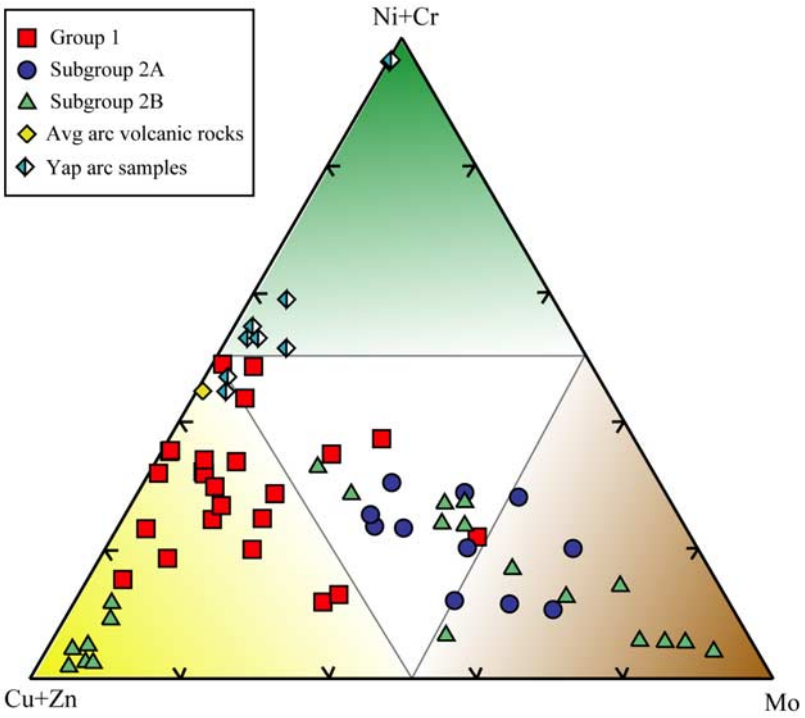

Figure 12. Discriminant ternary plot showing possible sources of trace metals in hydrothermal Mn deposits: Ni + Cr, leaching of ultramafic end-member; Cu + Zn, leaching of sulfide end-member, or nondeposition of sulfides at depth; Mo, high-temperature leaching of intermediate to acidic volcanic arc rocks; many samples fall along a line connecting the average arc volcanic rock (unleached; Table 6) with the high-temperature leaching apex characterized by relatively high Mo contents in the hydrothermal Mn. Most samples show a mixture of the Mo proxy and sulfide proxy end-members, which is more pronounced if Ni is not plotted with Cr, because Ni can have multiple sources (see text for discussion). Only the Yap samples have a strong contribution from ultramafic rocks (Yap arc samples from *Hein et al.* [1992]).

also occurs in sulfides and therefore has multiple sources; if high Ni is not accompanied by high Cr, then an ultramafic component may not be indicated. High Cu, Zn, Pb, and Cd concentrations predominantly reflect the influence of sulfides, such as whether sulfides were precipitated at depth and if so whether they were later leached by the fluids that precipitated the Mn oxides. Most of the Mn sandstones and a set of seven Zn-rich stratabound Mn samples reflect the dominant influence of sulfides (Figure 12); these samples may in addition represent a high-temperature end-member. The status of sulfides in the hydrothermal system seems to play a key role in the composition of the Mn oxide end-member (Figure 12). A proxy for the leaching of intermediate to silicic arc rocks might be the high Mo concentrations in many of our stratabound Mn samples (Figure 12). In basaltic systems, high Mo concentrations in the hydrothermal fluids reflect leaching only at high temperatures (>310°C); this Mo may be incorporated primarily into sulfides at depth [*Trefry et al.*, 1994]. If this scenario also holds for the IBM, then Mo, like Cu and Zn, would reflect the status of sulfides in the system. The fact that Mo does not correlate with Cu and Zn in our samples may indicate that it was not predominantly sequestered by sulfides at depth, as is also probably true for the Co in our samples. Both Mo and Co can be enriched in sulfides, but they may also reflect the high-temperature leaching of arc rocks, which we favor as an explanation for the high Mo and Co in our samples. Li may be a better discriminant element in place of Mo (Figure 12), but we do not have enough Li data to test that idea. High Ba concentrations in Mn oxides probably reflect either the leaching of organic-rich biogenic sediments (minor components of the Fe, Co, Ni, Cu, and Zn may also be from such a source), or the lack of precipitation of barite at depth in the hydrothermal systems. Our samples generally show relatively low Ba concentrations; leaching of biogenic sediments may therefore not have contributed significantly to the compositions of the IBM samples, except on a local scale as mentioned above for the enrichment of Ca related to the replacement of biocarbonate.

[80] A surprising result is that the proportion of hydrothermal Fe to silicate-associated Fe remains nearly constant regardless of Mn content, deposit type, or location; whereas the absolute amounts of the two sources of Fe increase with decreasing Mn in the deposits. This indicates that, although hydrothermal Fe occurs in all samples, it comprises a significant contribution relative to Mn content only in the Mn sandstones. This probably indicates higher temperatures and somewhat lower Eh conditions during formation of the Mn cements relative to the stratabound layers. The rocks with the highest Fe contents are strongly altered and this also indicates that mineralization of those Mn sandstones took place from relatively higher temperature fluids.

5.3. Seabed Mounds

[81] We suggest that water-saturated red hydrothermal muds formed mounds on the seabed and Mn oxides were deposited within the mounds as irregularly shaped, stratabound masses: the mounds provided a matrix within which the stratabound Mn oxides precipitated. Although we have no direct evidence for seabed hydrothermal mounds on the volcanoes sampled, their existence is inferred from the red muds recovered with a few hydrothermal Mn samples. The hydrothermal red muds were not recovered in great quantities, probably because they were washed out as the dredge hauls were brought up through the water column. Such mounds were observed during submersible dives in the Izu-Bonin arc [*Usui and Nishimura*, 1992a, 1992b] and have been described from other areas as well [e.g., *Kimura et al.*, 1988; *Hein et al.*, 1991]. On the basis of textures and lithologic associations, some of the stratabound Mn oxide deposits recovered in IBM dredges D3, D20, and D28 probably formed as the ascending mineralizing fluids arrived near the seawater/sediment interface. Electron microprobe determined Na and Mg concentrations of sample D3-3 support the interpretation of a near-seabed environment of formation for that sample. This order of precipitation would have been promoted by a decrease in temperature and increase in pH and/or Eh following deposition of the Fe oxyhydroxide. The morphology of this type of Mn oxide is quite different than the tabular stratiform layers found associated with the clastic rocks. These presumed mound deposits have some characteristics in common and some that contrast with Mn oxide deposits from the Galapagos mounds, a series of off-axis structures on the flank of the Galapagos spreading center. In the Galapagos mounds, Mn oxide formed first, near the surface of the mound, followed by nontronite which partly replaced the Mn oxide [*Honnorez et al.*, 1981]. Slightly reducing conditions promoted the formation of nontronite rather than Fe oxyhydroxide. The textures of the Mn oxide deposits from the Galapagos mounds are similar to those of the stratabound deposits recovered in dredge hauls D3, D20, and D28 and similarly indicate precipitation from an up-flow system and decreasing age with increasing depth in the sediment; numerous pulses of hydrothermal fluids were required to form the Mn oxides, rather than formation during continuous flow [*Moore and Vogt*, 1976; *Corliss et al.*, 1978; *Lalou et al.*, 1983].

5.4. Preservation in the Geologic Record and On-Land Analogs

[82] The preservation potential of an undissected oceanic volcanic arc is poor. Volcanic arcs can be obducted, subducted, or accreted during closure of back-arc basins or collision of arcs with continents. Tectonic processes are likely to obliterate the volcaniclastic sedimentary sequences and associated Mn oxide accumulations of the arc, as are sedimentary and volcanic processes (eruptions, erosion, mass wasting, slumping, etc.) prior to destruction of the arc. In addition, subsequent sedimentary or volcanic burial of the Mn oxides can produce reducing conditions that would remobilize the Mn. Although the preservation potential for these deposits is low, fossil analogs of IBM Mn oxide-type deposits occur on the Philippine Islands [*Sorem*, 1956], Todoro district Hokkaido, Japan; Eua and Tonumea Islands in Tonga [*Hein et al.*, 1991], on many of the islands in other volcanic arcs of the western Pacific, Mediterranean Sea [*Hein et al.*, 2000], and eastern Indian Ocean, on Cuba, and accreted terranes in Alaska, among others. Mn oxides that occur on the Yap Islands and Babeldoab Island (Belau), south of the Mariana Islands, have chemical compositions very similar to the Mariana stratabound Mn deposits (J. R. Hein, unpublished data, 1992).

[83] The lateral and vertical extents of the IBM arc Mn deposits are not known. Although Mn oxides were recovered along the length of the IBM arc, many of the individual deposits may be fairly small, with maximum dimensions of a few square kilometers and a few tens of meters stratigraphically being mineralized. Perhaps the best described analog to our IBM deposits is the Quaternary hydrothermal Mn deposit on Milos Island, Aegean arc, Greece. Hydrothermal fluids mineralized a series of volcaniclastic/pyroclastic rocks through cementation, formation of stratabound layers, and metasomatic replacement of a cap limestone in a shallow marine environment [*Hein et al.*, 2000]. A sediment body about 1 km long and 35 to 50 m thick was mineralized. About 35 to 40% of the beds in that section were mineralized, which supported mining operations for about 35 years during the late 1800s and early 1900s. The Milos deposit has higher Pb, Zn, As, Sb, Cu, and Cd contents than the IBM samples, perhaps as a result of greater leaching of sulfide deposits and the leaching of basement rock by high-salinity fluids produced by phase separation at depth on Milos [e.g., *Pflumio et al.*, 1993]. The Milos deposit may be a good indication of the size of deposits likely to be found along the IBM and other arc systems.

[84] **Acknowledgments.** We thank Lou Calk, U.S. Geological Survey, for help with the electron microprobe; Robert Oscarson, U.S. Geological Survey, for SEM support; and Herb Kirschenbaum, U.S. Geological Survey, for the ICP analyses. We thank Amy Draut and David Piper, U.S. Geological Survey, for helpful reviews of an early draft; and Geoffrey Glasby, Gary Massoth, and an anonymous reviewer for useful comments that improved the final paper.

References

Albee, A. L., and L. Ray (1970), Correction factors for electron-probe microanalysis of silicates, oxides, carbonates, phosphates and sulfates, *Anal. Chem.*, *42*(12), 1408–1414, doi:10.1021/ac60294a030.

Anders, E., and N. Grevesse (1989), Abundances of the elements: Meteoritic and solar, *Geochim. Cosmochim. Acta*, *53*(1), 197–214, doi:10.1016/0016-7037(89)90286-X.

Aruscavage, P. J., H. Kirschenbaum, and F. Brown (1989), Analytical methods: The determination of 27 elements in ferromanganese materials, in *Chemical Composition of Ferromanganese Crusts in the World Ocean: A Review and Comprehensive Database*, edited by F. T. Manheim and C. M. Lane-Bostwick, *U.S. Geol. Surv. Open File Rep.*, *89-020*, 44–53.

Baker, E. T., R. W. Embley, S. L. Walker, J. A. Resing, J. E. Lupton, K.-I. Nakamura, C. E. J. de Ronde, and G. J. Massoth (2008), Hydrothermal activity and volcano distribution along the Mariana arc, *J. Geophys. Res.*, doi:10.1029/2007JB005423, in press.

Bau, M., A. Koschinsky, P. Dulski, and J. R. Hein (1996), Comparison of the partitioning behaviours of yttrium, rare earth elements, and titanium between hydrogenetic marine ferromanganese crusts and seawater, *Geochim. Cosmochim. Acta*, *60*(10), 1709–1725, doi:10.1016/0016-7037(96)00063-4.

Bloomer, S. H., R. J. Stern, and N. C. Smoot (1989a), Physical volcanology of the submarine Mariana and volcano arcs, *Bull. Volcanol.*, *51*(3), 210–224, doi:10.1007/BF01067957.

Bloomer, S. H., R. J. Stern, E. Fisk, and C. H. Geschwind (1989b), Shoshonitic volcanism in the northern Mariana Arc: 1. Mineralogic and major and trace element characteristics, *J. Geophys. Res.*, *94*(B4), 4469–4496, doi:10.1029/JB094iB04p04469.

Bonatti, E., T. Kraemer, and H. Rydell (1972), Classification and genesis of submarine iron-manganese deposits, in *Ferromanganese Deposits on the*

Ocean Floor, edited by D. R. Horn, pp. 149–166, Natl. Sci. Found., Washington, D. C.

Boyd, T., S. D. Scott, and R. Hekinian (1993), Trace element patterns in Fe-Si-Mn oxyhydroxides at three hydrothermally active seafloor regions, *Resour. Geol., Spec. Issue*, *17*, 83–95.

Burns, R. G., and V. M. Burns (1977), Mineralogy, in *Marine Manganese Deposits, Elsevier Oceanography Series*, vol. 15, edited by G. P. Glasby, pp. 185–248, Elsevier, New York.

Burton, K. W., B. Bourdon, J.-L. Birck, C. J. Allègre, and J. R. Hein (1999), Osmium isotope variations in the oceans recorded by Fe-Mn crusts, *Earth Planet. Sci. Lett.*, *171*, 185–197, doi:10.1016/S0012-821X(99)00139-9.

Chan, L.-H., and J. R. Hein (2007), Lithium contents and isotopic compositions of ferromanganese deposits from the global ocean, *Deep Sea Res., Part II*, *54*, 1147–1162, doi:10.1016/j.dsr2.2007.04.003.

Corliss, J. B., M. Lyle, J. Dymond, and K. Crane (1978), The chemistry of hydrothermal mounds near the Galapagos rift, *Earth Planet. Sci. Lett.*, *40*, 12–24, doi:10.1016/0012-821X(78)90070-5.

Cowen, J. P., G. J. Massoth, and E. T. Baker (1986), Bacterial scavenging of Mn and Fe in a mid- to far-field hydrothermal particle plume, *Nature*, *322*, 169–171, doi:10.1038/322169a0.

Cowen, J. P., G. J. Massoth, and R. A. Feely (1990), Scavenging rates of dissolved manganese in a hydrothermal vent plume, *Deep Sea Res., Part A*, *37*, 1619–1637, doi:10.1016/0198-0149(90)90065-4.

Cronan, D. S., G. P. Glasby, S. A. Moorby, J. Thomson, K. E. Knedler, and J. C. McDougall (1982), A submarine hydrothermal manganese deposit from the south-west Pacific island arc, *Nature*, *298*, 456–458, doi:10.1038/298456a0.

Cronan, D. S., R. Hodkinson, and T. D. S. Rogers (2002), Diagenetically modified buried hydrothermal manganese crusts from the Lau Basin, S.W. Pacific, *Mar. Georesour. Geotechnol.*, *20*, 51–72, doi:10.1080/106411902753556852.

Dickinson, W. R., L. S. Beard, G. R. Brakenridge, J. L. Erjavec, R. C. Ferguson, K. F. Inman, R. A. Knepp, F. A. Lindberg, and P. T. Ryberg (1983), Provenance of North American Phanerozoic sandstones in relation to tectonic setting, *Geol. Soc. Am. Bull.*, *94*, 222–235, doi:10.1130/0016-7606(1983)94<222:PONAPS>2.0.CO;2.

Draut, A. E., and P. D. Clift (2006), Sedimentary processes in modern and ancient oceanic arc settings: Evidence from the Jurassic Talkeetna Formation of Alaska and the Mariana and Tonga arcs, western Pacific, *J. Sediment. Res.*, *76*, 493–514, doi:10.2110/jsr.2006.044.

Engleman, E. E., L. L. Jackson, and D. R. Norton (1985), Determination of carbonate carbon in geological materials by coulometric titration, *Chem. Geol.*, *53*, 125–128, doi:10.1016/0009-2541(85)90025-7.

Fitzgerald, C. E., and K. M. Gillis (2006), Hydrothermal manganese oxide deposits from Baby Bare seamount in the northeast Pacific Ocean, *Mar. Geol.*, *225*, 145–156, doi:10.1016/j.margeo.2005.09.005.

Gavrilenko, G. M. (1997), *Under-water Volcanic and Hydrothermal Activity as a Source of Metals in the Ferromanganese Formations of the Island Arcs* (in Russian), 165 pp., Dal'nauka, Vladivostok, Russia.

Glasby, G. P., D. Stüben, G. Jeschke, P. Stoffers, and C.-D. Garbe-Schönberg (1997), A model for the formation of hydrothermal manganese crusts from the Pitcairn Island hotspot, *Geochim. Cosmochim. Acta*, *61*, 4583–4597, doi:10.1016/S0016-7037(97)00262-7.

Glasby, G. P., G. A. Cherkashov, G. M. Gavrilenko, V. A. Rashidov, and I. B. Slovtsov (2006), Submarine hydrothermal activity and mineralization on the Kurile and western Aleutian island arcs, N.W. Pacific, *Mar. Geol.*, *231*, 163–180, doi:10.1016/j.margeo.2006.06.003.

Halbach, P., M. Segl, D. Puteanus, and A. Mangini (1983), Co-fluxes and growth rates in ferromanganese deposits from central Pacific seamount areas, *Nature*, *304*, 716–719, doi:10.1038/304716a0.

Hein, J. R. (2004), Cobalt-rich ferromanganese crusts: Global distribution, composition, origin and research activities, in *Workshop on Minerals Other than Polymetallic Nodules of the International Seabed Area*, vol. 1, pp. 188–256, Int. Seabed Auth., Kingston, Jamaica.

Hein, J. R., C. L. Fleishman, L. A. Morgenson, S. H. Bloomer, and R. J. Stern (1987), Submarine ferromanganese deposits from the Mariana and Volcano volcanic arcs, west Pacific, *U.S. Geol. Surv. Open File Rep.*, *87-281*, 67 pp.

Hein, J. R., M. S. Schulz, and L. A. Gein (1990), Central Pacific cobalt-rich ferromanganese crusts: Historical perspective and regional variability, in *Geology and Offshore Mineral Resources of the Central Pacific Basin*, *Earth Sci. Ser.*, vol. 15, edited by B. Keating and B. Bolton, pp. 261–283, Circum-Pac. Counc. for Energy and Miner. Resour., Houston, Tex.

Hein, J. R., M. S. Schulz, and J. K. Kang (1991), Insular and submarine ferromanganese mineralization of the Tonga-Lau region, *Mar. Mineral.*, *9*(3), 305–354.

Hein, J. R., et al. (1992), Geology, geophysics, geochemistry, and deep-sea mineral deposits, Federated States of Micronesia: KORDI-USGS R. V. *Farnella* cruise F11–90-CP, *U.S. Geol. Open File Rep.*, *92–218*, 191 pp.

Hein, J. R., A. E. Gibbs, D. A. Clague, and M. Torresan (1996), Hydrothermal mineralization along submarine rift zones, Hawaii, *Mar. Georesour. Geotechnol.*, *14*, 177–203.

Hein, J. R., A. Koschinsky, P. Halbach, F. T. Manheim, M. Bau, J.-K. Kang, and N. Lubick (1997), Iron and manganese oxide mineralization in the Pacific, in *Manganese Mineralization: Geochemistry and Mineralogy of Terrestrial and Marine Deposits*, edited by K. Nicholson et al., *Geol. Soc. Spec. Publ.*, *119*, 123–138.

Hein, J. R., et al. (1999), Co-rich Fe-Mn crusts from the Marshall Islands (Leg 1) and hydrothermal and hydrogenetic Fe-Mn deposits from Micronesia (Leg 2), KODOS 98–3 cruise, west Pacific, *U.S. Geol. Surv. Open File Rep.*, *99–412*, 63 pp.

Hein, J. R., M. G. Stamatakis, and J. S. Dowling (2000), Trace metal-rich Quaternary hydrothermal manganese oxide and barite deposit, Milos Island, Greece, *Trans. Inst. Mineral. Metall., Sect. B*, *109*, B67–B76.

Honnorez, J., et al. (1981), Hydrothermal mounds and young ocean crust of the Galapagos: Preliminary Deep Sea Drilling results, Leg 70, *Geol. Soc. Am. Bull.*, *92*(7), 457–472, doi:10.1130/0016-7606(1981)92<457:HMAYOC>2.0.CO;2.

Jackson, L. L., F. W. Brown, and S. T. Neil (1987), Major and minor elements requiring individual determination, classical whole rock analysis, and rapid rock analysis, in *Methods for Geochemical Analysis*, edited by P. A. Baedecker, *U.S. Geol. Surv. Bull.*, *1770*, G1–G23.

Kang, J.-K., and A. Kosakevitch (1984), *Etude textural des encroutements ferro manganesiferes de l'est Caraibe*, Bur. de Rech. Geol. et Min., Serv. Geol. Natl., Orleans, France.

Kimura, M., S. Uyeda, Y. Kata, T. Tanaka, M. Yamano, T. Gamo, H. Sakai, S. Kato, E. Izawa, and T. Oomori (1988), Active hydrothermal mounds in the Okinawa Trough backarc basin, Japan, *Tectonophysics*, *145*(3–4), 319–324, doi:10.1016/0040-1951(88)90203-X.

Kinoshita, M., Y. Kawada, A. Tanaka, and T. Urabe (2006), Recharge/discharge interface of a secondary hydrothermal circulation in the Suiyo Seamount of the Izu-Bonin arc, identified by submersible-operated heat flow measurements, *Earth Planet. Sci. Lett.*, *245*, 498–508, doi:10.1016/j.epsl.2006.02.006.

Klovan, J. E., and J. Imbrie (1971), An algorithm and FORTRAN-IV program for large-scale Q-mode factor analysis and calculation of factor scores, *Math. Geol.*, *3*, 61–77, doi:10.1007/BF02047433.

Koschinsky, A., and J. R. Hein (2003), Uptake of elements from seawater by ferromanganese crusts: Solid-phase associations and seawater speciation, *Mar. Geol.*, *198*, 331–351, doi:10.1016/S0025-3227(03)00122-1.

Kuhn, T., B. C. Bostick, A. Koschinsky, P. Halbach, and S. Fendorf (2003), Enrichment of Mo in hydrothermal Mn precipitates: Possible Mo sources, formation process and phase associations, *Chem. Geol.*, *199*, 29–43, doi:10.1016/S0009-2541(03)00054-8.

Lalou, C., E. Brichet, C. Jehanno, and H. Perez-Leclaire (1983), Hydrothermal manganese oxide deposits from Galapagos mounds, DSDP Leg 70, hole 509B and "Alvin" dives 729 and 721, *Earth Planet. Sci. Lett.*, *63*, 63–75, doi:10.1016/0012-821X(83)90022-5.

Lichte, F. E., D. W. Golightly, and P. J. Lamothe (1987a), Inductively coupled plasma-atomic emission spectrometry, in *Methods for Geochemical Analysis*, edited by P. A. Baedecker, *U.S. Geol. Surv. Bull.*, *1770*, B1–B10.

Lichte, F. E., A. L. Meier, and J. G. Crock (1987b), Determination of the rare earth elements in geological materials by inductively coupled plasma-mass spectrometry, *Anal. Chem.*, *59*(8), 1150–1157, doi:10.1021/ac00135a018.

Lin, P.-N., R. J. Stern, and S. H. Bloomer (1989), Shoshonitic volcanism in the northern Mariana Arc: 2. large-ion lithophile and rare earth element abundances: Evidence for the source of incompatible element enrichments in intraoceanic arcs, *J. Geophys. Res.*, *94*, 4497–4514, doi:10.1029/JB094iB04p04497.

Malahoff, A., I. Y. Kolotyrkina, B. P. Midson, and G. J. Massoth (2006), A decade of exploring a submarine intraplate volcano: Hydrothermal manganese and iron at Lô'ihi volcano, Hawai'i, *Geochem. Geophys. Geosyst.*, *7*, Q06002, doi:10.1029/2005GC001222.

Manceau, A., M. Lanson, and N. Geoffroy (2007), Natural speciation of Ni, Zn, Ba, and As in ferromanganese coatings on quartz using X-ray florescence, absorption, and diffraction, *Geochim. Cosmochim. Acta*, *71*, 95–128, doi:10.1016/j.gca.2006.08.036.

Manheim, F. T., and C. M. Lane-Bostwick (1988), Cobalt in ferromanganese crusts as a monitor of hydrothermal discharge on the Pacific seafloor, *Nature*, *335*, 59–62, doi:10.1038/335059a0.

McLennan, S. M. (1989), Rare earth elements in sedimentary rocks: Influence of provenance and sedimentary processes, in *Geochemistry and Mineralogy of Rare Earth Elements*, *Rev. Mineral.*, vol. 21, edited by B. R. Lipin and G. A. McKay, pp. 169–200, Mineral. Soc. of Am., Washington, D. C.

Mellin, T. A., and G. Lei (1993), Stabilization of 10 Å-manganates by interlayer cations and hydrothermal treatment: Implications for the miner-

alogy of marine manganese concretions, *Mar. Geol.*, *115*, 67–83, doi:10.1016/0025-3227(93)90075-7.

Moorby, S. A., D. S. Cronan, and G. P. Glasby (1984), Geochemistry of hydrothermal Mn-oxide deposits from the S.W. Pacific island arc, *Geochim. Cosmochim. Acta*, *48*, 433–441, doi:10.1016/0016-7037(84)90272-2.

Moore, W. S., and P. R. Vogt (1976), Hydrothermal manganese crusts from two sites near the Galapagos spreading axis, *Earth Planet. Sci. Lett.*, *29*, 349–356, doi:10.1016/0012-821X(76)90139-4.

Mottl, M. J. (1983), Metabasalts, axial hot springs, and the structure of hydrothermal systems at mid-ocean ridges, *Geol. Soc. Am. Bull.*, *94*, 161–180, doi:10.1130/0016-7606(1983)94<161:MAHSAT>2.0.CO;2.

Ostwald, J., and J. V. Dubrawski (1987), An X-ray diffraction investigation of a marine 10Å manganate, *Mineral. Mag.*, *51*, 463–466, doi:10.1180/minmag.1987.051.361.14.

Pflumio, C., L. Briqueu, J. Boulegue, and A. Liakopoulos (1993), Geochemical and isotopic characteristics of present-day and past geothermal systems of Milos Island (Aegean Arc), *Resour. Geol., Spec. Issue*, *16*, 50–53.

Rogers, T. D. S., R. A. Hodkinson, and D. S. Cronan (2001), Hydrothermal manganese deposits from the Tonga-Kermadec Ridge and Lau Basin region, southwest Pacific, *Mar. Georesour. Geotechnol.*, *19*, 245–268, doi:10.1080/106411901753335326.

Schulz, M. S., and J. R. Hein (1991), Petrography and chemistry of hydrothermal manganese oxyhydroxides from the Mariana and Izu-Bonin Volcanic arcs, West Pacific, *U.S. Geol. Surv. Open File Rep.*, *91-557*, 80 pp.

Scott, R. B., P. A. Rona, B. A. McGregor, and M. R. Scott (1974), The TAG Hydrothermal Field, *Nature*, *251*, 301–302, doi:10.1038/251301a0.

Shapiro, L. (1975), Rapid analysis of silicate, carbonate, and phosphate rocks—Revised edition, *U.S. Geol. Surv. Bull.*, *1401*, 76 pp.

Sorem, R. K. (1956), Geology of three major manganese districts of the Philippines, in *Proceedings of the Pacific Science Congress*, vol. II-A, pp. 661–668, Natl. Res. Counc. of the Philippines, Univ. of the Philippines, Quezon City.

Thompson, G., M. J. Mottl, and P. A. Rona (1985), Morphology, mineralogy and chemistry of hydrothermal deposits from the TAG area, 26°N Mid-Atlantic Ridge, *Chem. Geol.*, *49*, 243–257, doi:10.1016/0009-2541(85)90159-7.

Trefry, J. H., D. B. Butterfield, S. Metz, G. J. Massoth, R. P. Trocine, and R. A. Feely (1994), Trace metals in hydrothermal solutions from Cleft segment on the southern Juan de Fuca Ridge, *J. Geophys. Res.*, *99*, 4925–4935, doi:10.1029/93JB02108.

Usui, A., and A. Nishimura (1992a), Submersible observations of hydrothermal manganese deposits on the Kaikata Seamount, Izu-Ogasawara (Bonin) Arc, *Mar. Geol.*, *106*, 203–216, doi:10.1016/0025-3227(92)90130-A.

Usui, A., and A. Nishimura (1992b), Hydrothermal manganese oxide deposits from the Izu-Ogasawara (Bonin)-Mariana Arc and adjacent areas, *Bull. Geol. Surv. Jpn.*, *43*, 257–284.

Usui, A., M. Yuasa, S. Yokota, M. Nohara, A. Nishimura, and F. Murakami (1986), Submarine hydrothermal manganese deposits from the Ogasawara (Bonin) Arc, off the Japan Islands, *Mar. Geol.*, *73*, 311–322, doi:10.1016/0025-3227(86)90020-4.

Usui, A., T. A. Mellin, M. Nohara, and M. Yuasa (1989), Structural stability of marine 10 Å manganates from the Ogasawara (Bonin) Arc: Implication for low-temperature hydrothermal activity, *Mar. Geol.*, *86*, 41–56, doi:10.1016/0025-3227(89)90017-0.

S. H. Bloomer, College of Science, Oregon State University, 128 Kidder Hall, Corvallis, OR 97331-4608, USA. (sherman.bloomer@oregonstate.edu)

R. E. Dunham, J. R. Hein, and M. S. Schulz, U.S. Geological Survey, 345 Middlefield Road, Menlo Park, CA 94025, USA. (rdunham@usgs.gov; jhein@usgs.gov; mschulz@usgs.gov)

R. J. Stern, Geosciences Department, University of Texas at Dallas, Richardson, TX 75080-3021, USA. (rjstern@utdallas.edu)